Scalable Apparatus to Measure Posture and Locomotion (SAMPL): a high-throughput solution to study unconstrained vertical behavior in small animals

Yunlu Zhu[1,2,3] **Franziska Auer**[1,2,3] **Hannah Gelnaw**[1,2,3] **Samantha N. Davis**[1,2,3] **Kyla R. Hamling**[1,2,3] **Christina E. May**[2,3] **Hassan Ahamed**[4] **Niels Ringstad**[4] **Katherine I. Nagel**[2,3] **David Schoppik**[1,2,3,5,*]

[1]Department. of Otolaryngology, New York University Grossman School of Medicine
[2]The Neuroscience Institute, New York University Grossman School of Medicine
[3]Department of Neuroscience & Physiology, New York University Grossman School of Medicine
[4]Department of Cell Biology, Skirball Institute of Biomolecular Medicine, New York University Grossman School of Medicine
[5]Lead Contact
[*]Correspondence: schoppik@gmail.com

1   **ABSTRACT**

2   **Balance and movement are impaired in a wide variety of neurological disorders. Recent**

3   **advances in behavioral monitoring provide unprecedented access to posture and loco-**

4   **motor kinematics, but without the throughput and scalability necessary to screen can-**

5   **didate genes / potential therapeutics. We present a powerful solution: a Scalable Appa-**

6   **ratus to Measure Posture and Locomotion (SAMPL). SAMPL includes extensible imag-**

7   **ing hardware and low-cost open-source acquisition software with real-time processing.**

8   **We first demonstrate that SAMPL's hardware and acquisition software can acquire data**

9   **from *D. melanogaster*, *C.elegans*, and *D. rerio* as they move vertically. Next, we lever-**

10   **age SAMPL's throughput to rapidly (two weeks) gather a new zebrafish dataset. We use**

11   **SAMPL's analysis and visualization tools to replicate and extend our current understand-**

12   **ing of how zebrafish balance as they navigate through a vertical environment. Next, we**

13   **discover (1) that key kinematic parameters vary systematically with genetic background,**

14   **and (2) that such background variation is small relative to the changes that accompany**

15   **early development. Finally, we simulate SAMPL's ability to resolve differences in posture**

16   **or vertical navigation as a function of effect size and data gathered – key data for screens.**

17   **Taken together, our apparatus, data, and analysis provide a powerful solution for labora-**

18   **tories using small animals to investigate balance and locomotor disorders at scale. More**

19   **broadly, SAMPL is both an adaptable resource for laboratories looking process video-**

20   **graphic measures of behavior in real-time, and an exemplar of how to scale hardware to**

21   **enable the throughput necessary for screening.**

22 INTRODUCTION

23 Measuring posture and locomotion is key to understand nervous system function and evalu-
24 ate potential treatments for disease – particularly neurological disorders[1]. Behavioral screen-
25 ing is a fundamental part of both basic and translational approaches to disease[2,3]. For screens,
26 measuring behavior from large numbers of animals is necessary to differentiate individual vari-
27 ation[4] from changes seen in disease models and/or improvement following treatment[5,6]. The
28 demand for such high-throughput measurements comes at a cost: often, measurements that
29 require high resolution – such as posture – are limited. Modern machine learning algorithms
30 and inexpensive videographic / computing hardware have automated measurements of pos-
31 ture and kinematics[7–9] and illuminated our understanding of animal behavior[10–12]. We sought
32 to combine videographic analysis of posture and vertical locomotion with the scalability amenable
33 to screening.

34 Over the past decade, we have studied posture and locomotion using the larval zebrafish as a
35 model. Neural architecture is highly conserved across vertebrates, making larval zebrafish an
36 excellent model to understand the underpinnings of locomotion[13,14] and balance[15]. For our
37 studies, we developed a new apparatus/analysis pipeline to measure the statistics of posture
38 in the pitch (nose-up/nose-down) axis and locomotion as larvae swam freely in depth. We dis-
39 covered that larvae learn to time their movements to facilitate balance[16], that larvae modulate
40 the kinematics of swimming to correct posture[17], and that larvae engage their pectoral fins to
41 climb efficiently[18], and implicated different neuronal circuits in each of these behaviors. While
42 informative, data collection was slow (months) on small numbers (<5) of apparatus. Increasing
43 throughput remains a challenge common to laboratories that develop new tools to measure
44 behavior.

45 To meet the needs of scalability, resolution, and extensibility we developed SAMPL: a low-cost,
46 open-source solution that measures posture and vertical locomotion in real-time in small an-
47 imals. Further, we provide a turn-key analysis pipeline to measure larval zebrafish balance be-
48 havior. We begin with a brief treatment of the hardware and software; a detailed design guide,
49 assembly and operating instructions are included as supplemental appendices. Next, we use
50 SAMPL to measure unconstrained vertical locomotion in two common invertebrate models:
51 flies (*Drosophila melanogaster*), and worms (*Caenorhabditis elegans*), as well as a small model
52 vertebrate, the larval zebrafish (*Danio rerio*). To illustrate SAMPL's capabilities, we parameterize
53 a new dataset focused on behaviors that larval zebrafish perform as they stabilize posture and

54   navigate (i.e. climb/dive) in the water column. Our new dataset represents two weeks worth

55   of data collection, and allowed us to detail variation in postural/locomotor behaviors. By mea-

56   suring behavior across different genetic backgrounds and development, we report two new

57   findings. First, variation in posture/locomotion is systematic across genotype and second, the

58   scale of variation in behavior across development is much larger than background genetic

59   variation. We use these new data to simulate the resolving power for each behavioral param-

60   eter as a function of data gathered – foundational information to rigorously assay the effects of

61   candidate genes or small molecules on posture or locomotion. SAMPL thus offers a straight-

62   forward way to gather data from small animals, and a turn-key solution to screen for balance

63   and vertical locomotion in larval zebrafish. More broadly, SAMPL offers a template for labora-

64   tories looking to scale their own behavioral apparatus to achieve the throughput necessary for

65   screens. SAMPL will thus facilitate reproducible studies of postural and locomotor behaviors in

66   both health and disease, addressing unmet needs in treating neurological disorders, particu-

67   larly with balance symptoms [19].

68   **RESULTS**

69   **SAMPL hardware & software overview**

70   To overcome measure posture with the throughput necessary for genetic and drug screens,

71   we deployed SAMPL, a real-time videographic system (Figure 1A) that records small animal

72   behavior in the vertical axis. Below we briefly describe the hardware and software that com-

73   prise SAMPL. SAMPL's hardware consists of three simple modules: an infrared (IR) illumination

74   module (Figure 1B), a camera-lens module (Figure 1C), and two clamps to hold fish chambers

75   (Figure 1D). All three modules are mounted directly (Figure 1A) onto an aluminum breadboard

76   (Figure S1) and a light-tight enclosure covers the entire apparatus to permit individual control

77   of lighting (Figures 1F and 1G). Details of hardware and software design can be found in Ap-

78   pendices 1&2. A complete parts list is in Table 1, hardware assembly instructions in Appendix

79   3, and a stop-motion movie of assembly provided as Movie 1.

80   The IR module illuminates the arena from behind. It is optimized to fulfill four criteria: (1) high

81   image quality; (2) a large area for imaging; (3) imperceptible illumination; (4) ample heat dis-

82   sipation. We used a 940 nm "star" style LED as our source of IR illumination and developed a

83   simple illumination module to diffuse IR light across a 50mm circle (Figure 1B). For heat man-

84   agement, each LED was mounted to a small heat sink (Figure 1B). This setup allows us to power

85   three illumination modules in series using a single LED driver.

86 The second module captures videographic data. It consists of a camera and lens optimized for
87 speed, resolution, compactness, and affordability. The camera hardware satisfies the follow-
88 ing demands: (1) large pixel size with low noise allowing for high dynamic range / signal-to-
89 noise ratio; (2) sufficient resolution to resolve subtle changes to animal posture; (3) an interface
90 with sufficient bandwidth for data transfer; (4) availability. The lens achieves (1) close focus; (2)
91 sufficient depth-of-field to cover the entire depth of the imaging arena; (3) high image qual-
92 ity; (4) compact size; (5) high IR transmission rate; (6) ease of integrating an IR-pass filter. We
93 adapted a 50 mm IR-optimized lens by placing a 0.3" extension tube between the lens and
94 the camera to achieve higher magnification ratio with minimum working distance. The space
95 between camera adapters and the extension tube allows us to fit a 25 mm IR-pass filter; the
96 extension tube gives a mount point to connect the module to the base (Figure 1A). Using this
97 camera-lens module, we image an area ~400 mm^2 (Figure 1E, pink square) at 166 Hz with
98 1200×1216 pixels at a focal distance of ~24 cm.

99 The final module is a rectangular arena optimized for vertical locomotion (i.e. parallel to the
100 focal plane). By design, the chamber size is larger than the imaging area, allowing stochastic
101 sampling of freely behaving animals in a large enough arena. The bottom of the chamber is
102 below the field of view so that animals sitting at the bottom will not be recorded. We assem-
103 bled custom-fabricated chambers from laser-cut acrylic by cementing transparent front and
104 back sides to a U-shaped piece that forms the narrower sides (Figure 1E). We designed two
105 types of chambers with different inner widths to adapt to the needs of different experiments:
106 a wider standard chamber optimized for larger groups of animals and a narrower chamber for
107 1-3 animals (Figure 1E). Chambers can be easily dropped into the holders (Figure 1D) from the
108 top of the behavior box and secured in place for recording.

109 SAMPL includes a complete suite of open-source software for acquisition/real-time extraction
110 of data (source and compiled executables provided). Acquisition consists of a graphical user in-
111 terface, written in LabView that analyzes video in real-time to isolate an animal's location and
112 orientation, with the ability to save raw video for further off-line analysis. The real-time process-
113 ing algorithm consists of: (1) background subtraction; (2) noise thresholding; (3) rejection of
114 frames without an animal or with >1 animal in view; (4) size and intensity criteria to identify two
115 distinct animal parts, usually the body and the head; (5) image processing to extract location
116 and body orientation relative to the horizon. Data about location and orientation is saved to a
117 text file, metadata about the experiment is saved to a separate text file, and optionally, video is

118 saved as an AVI file.

119 SAMPL's modules and software were designed to scale, minimizing footprint and experimenter

120 time. We multiplex apparatus, providing three distinct compiled applications designed to run

121 simultaneously on one computer to reduce cost/footprint. A set of three SAMPL apparatus and

122 a computer case fit on one 24"x36" shelf (Figure 1H). One SAMPL "rack" consists of four such

123 shelves (81.5" high) and costs ~$40,000-$45,000 (December 2022, before volume discounts).

124 In our laboratory, trained experimenters can load such a rack for a typical 48 hr experiment in

125 30 minutes. Taken together, SAMPL's design is ideal to efficiently gather data describing pos-

126 ture and vertical locomotion.

SAMPL validation: different small animals

128 SAMPL is well-suited to collect data from a wide range of small animals. We demonstrate the

129 flexibility of SAMPL's acquisition suite using three common model organisms. By changing

130 SAMPL's thresholds (Table 2), we could acquire data from three different organisms: *Drosophila*

131 *melanogaster* climbing behavior (Figures 2A and 2B), continuous locomotion in *Caenorhabdi-*

132 *tis elegans* (Figures 2C and 2D), and swimming in *Danio rerio* (Figures 2E and 2F). We present

133 raw video from the epochs in Figure 2 together with plots of real-time image processing (fly &

134 worms, Movie 2; fish, Movie 3). These results demonstrate SAMPL's excellent flexibility and ro-

135 bustness in real-time recording and analysis of vertical locomotion of small animals.

SAMPL validation: measuring postural and locomotor kinematics in real-time

137 Next, to demonstrate how SAMPL facilitates efficient collection of high-quality kinematic data,

138 we gathered a new dataset from larval zebrafish (7-9 days post-fertilization, dpf) that swam

139 freely in the dark. A typical experimental repeat consisted of two sequential 24-hour sessions

140 using 3 SAMPL boxes. Data were pooled across 27 repeats for subsequent analysis of kine-

141 matics. Each 24-hour behavior session yielded on average 1223±481 bouts per day for the

142 standard chamber (6-8 fish) and 1251±518 bouts per day for the narrow chamber (1-3 fish).

143 While not analyzed, running a single fish in the narrow chamber yielded 891±903 bouts over

144 24hrs. Based on the number of apparatus used, we estimate that a similar dataset (total n=121,979

145 bouts) could be collected in **two weeks** using a single SAMPL rack.

146 We first used our data to establish basic distributions of locomotion and posture. We used SAMPL's

147 processing algorithm to extract the following information in real-time: (1) pitch, defined as the

148 angle between the long axis of the fish's body and the horizon (Figure 2E); (2) x (azimuth), z

149 (elevation) coordinates of the center of the pixels that correspond to the fish. After collection,

150   we used SAMPL's processing suite to extract basic postural kinematics during swimming. Ze-

151   brafish larvae swim in discrete periods of translation called "swim bouts" (Figure 2F) [16,20]. We

152   defined swim bouts as periods where the instantaneous speed exceeds 5 mm/sec (Figure 2F,

153   dashed line). The time of the peak speed was defined as t = 0 ms (Figure 2F, cyan lines). Swim

154   bouts were aligned to peak speed for extraction of kinematic parameters; the period 250 ms

155   before and 200 ms after peak speed was reserved for future analysis. We observed that ze-

156   brafish larvae swim predominantly at slower speeds with mean and standard deviation mea-

157   sured 12.90±4.91 mm/s, on par with previous reports [16,20–22]. Larvae showed a broad distri-

158   bution of postures evaluated at peak speed (8.48°±15.23°) with a positive (nose-up) average,

159   suggesting that SAMPL detected a variation of nose-up and nose-down swim bouts. SAMPL

160   can thus rapidly acquire a rich dataset of spontaneous locomotor behavior and a wide range of

161   "natural" postures.

162   **SAMPL validation: extracting key parameters of balance and vertical navigation in zebrafish**

163   SAMPL includes data analysis and visualization code (Python source and sample datasets pro-

164   vided) optimized to extract key parameters of balance and locomotion from larval zebrafish.

165   We use our "two-week" dataset to demonstrate that SAMPL can resolve these four parameters:

166   Figure 3: Control of movement timing. [16]

167   Figure 4: Control of steering to climb/dive. [17]

168   Figure 5: Coordination between trunk and fin. [18]

169   Figure 6: Control of posture stabilizing rotations. [17]

170   We conclude that SAMPL's resolution and throughput allows rapid and deep insight into each

171   parameter, detailed below. Data analysis using the provided scripts on the provided dataset

172   runs in 30 minutes on a typical analysis computer (M1 processor, 16GB RAM). Full details of

173   analysis/visualization is provided in Appendix 4, and a step-by-step guide to set up the relevant

174   environment and to run experiments provided in Appendix 5.

175   Proper balance requires active stabilization. Zebrafish larvae are front-heavy and therefore sub-

176   ject to destabilizing torques in the pitch (nose-up/nose-down) axis. Swim bouts counteract the

177   resultant forces, stabilizing the fish. Zebrafish larvae learn to initiate swim bouts when unsta-

178   ble [16]. We first defined movement rate as the reciprocal of the inter-bout interval (Figures 3A

179   and 3B). More extreme postures were associated with higher movement rate (Figure 3C), with

180   a parabolic relationship (Figure 3D, R^2 = 0.14). We expect that the majority of the residual vari-

181   ance reflects a previously-reported dependence of movement timing on angular velocity [16].

182 The three coefficients of the parabola represent the baseline posture, the basal rate of move-

183 ment, and – key to our analysis – the degree to which postural eccentricity relates to movement

184 rate, or "sensitivity," (Figure 3D). SAMPL therefore permits efficient quantification of a crucial

185 posture-stabilizing behavior: the relationship between perceived instability and corrective be-

186 havior.

187 Like most animals, larval zebrafish go where their head points. To adjust their vertical trajec-

188 tory (i.e. to climb or dive) larvae must rotate their bodies away from their initial posture, point-

189 ing in the direction they will travel (Figures 4A and 4B)[17,23]. Previous work[17] established that

190 steering rotation in larvae swimming spontaneously occurs mostly before they reach the peak

191 speed (Figure 4C). A larva's steering ability reflects the relationship between the change in pos-

192 ture before the peak speed and the resultant deviation in trajectory (Figure 4D). We parame-

193 terized steering as the slope (gain) of the best-fit line between posture and trajectory evaluated

194 at the time of peak speed (Figure 4E). A gain of 1 indicates that the observed trajectory could

195 be explained entirely by the posture at the time of peak speed (Figure 4F). SAMPL revealed

196 that 7 dpf larvae exhibit an average steering gain at 0.67, suggesting an offset between pos-

197 ture and trajectory at the time of peak speed (Figure 4E, R^2 = 0.92). SAMPL allows us to infer

198 how effectively larvae steer using axial (trunk) musculature to navigate the water column.

199 To climb (Figures 5A and 5B) fish generate lift with their pectoral fins, assisting steering rota-

200 tions and subsequent axial undulation[24,25]. Larval zebrafish learn to climb efficiently by coor-

201 dinating their trunk and fins[18]. We defined the attack angle, or the additional lift associated

202 with each climb, as the difference between the steering-related changes and the resulting tra-

203 jectory (Figure 5C). We evaluated attack angle after pectoral fin loss, revealing a clear contribu-

204 tion to climbs (Figure 5D). Next, we demonstrate a positive correlation (with rectification and

205 asymptote) between steering-related rotations and fin-based attack angle (Figure 5E, left). No-

206 tably, after peak angular velocity, rotations are poorly correlated with attack angles (r = -0.17)

207 (Figure 5E, right). These residuals reflect the initial angular deceleration as fish reach their peak

208 speed (Figure 5A). We parameterize the relationship between the initial rotation and the attack

209 angle using logistic regression (Figure 5F, R^2 = 0.31). The regression reveals the maximal slope

210 of the sigmoid relating steering and lift (Figure 5G). We named this slope "fin-body ratio" as it

211 describes how larvae distribute labor between axial and appendicular muscles, i.e. between

212 trunk (steering) and fins (lift), as shown in previous work[18]. SAMPL thus permits efficient infer-

213 ence of coordinated behavior.

214 Larvae must actively maintain their preferred posture in the pitch axis. To do so, they rotate

215 partially towards their preferred orientation as they decelerate (Figures 6A to 6C). The magni-

216 tude of these rotations scales with the eccentricity of their posture before a swim bout[17]. We

217 estimated the slope (-0.17) of the line that related initial posture and the amount the fish ro-

218 tated back toward the horizontal (Figure 6D), R^2 = 0.56. As the behavior is corrective, the re-

219 lationship is negative; we therefore define the gain of righting as the inverse of the slope (Fig-

220 ure 6E). We further define the "set point" as the point where an initial posture would be ex-

221 pected to produce a righting rotation of zero (Figures 6E and 6F). SAMPL facilitates quantifi-

222 cation of corrective reflex abilities (gain) and associated internal variables (set point).

223 Taken together, our estimates of key posture and locomotor parameters establish that SAMPL

224 can rapidly generate datasets that permit rich insight into the mechanisms of balance and ver-

225 tical navigation.

226 **SAMPL can resolve slight variations in posture control strategies across genetic backgrounds**

227 To be useful SAMPL must resolve small but systematic differences in key measures of posture

228 and vertical locomotion. Even among isogenic animals reared in controlled environments, ge-

229 netic differences contribute to behavioral variability[26–33]. The "two-week" dataset analyzed

230 in Figures 3 to 6 included data from three different genetic backgrounds. Larvae for experi-

231 ments were generated by crossing the same clutch of wild-type adults (mixed background)

232 to zebrafish of three different strains: AB (n = 62457 bouts, N = 225 fish over 10 experimen-

233 tal repeats); SAT (n = 27990 bouts, N = 117 fish over 7 experimental repeats); and the lab wild

234 type (n = 31532 bouts, N = 195 fish over 10 experimental repeats), which resembles real-world

235 approaches where a key transgenic line is often crossed to different backgrounds for experi-

236 ments. To capture the full variance in the dataset, we took a conservative approach by calcu-

237 lating kinematic parameters for individual experimental repeats (n = 4518±1658 bouts). We

238 assayed SAMPL's sensitivity by asking (1) if there were detectable differences in the four pa-

239 rameters defined in Figures 3 to 6 and (2) if these differences were systematic.

240 Qualitatively, larval zebrafish of the same age swim similarly; as expected, the magnitude of

241 change across strains we observed in Figure 7 is quite small. Nonetheless SAMPL could resolve

242 systematic variations in locomotion behavior and balance abilities among larvae of different

243 strains (Figure 7). AB larvae exhibited the best posture stability, demonstrated by the lowest

244 standard deviation of IBI pitch compared to the other two strains (Figure 7C). Correspondingly,

245 AB larvae had the highest bout frequency (Figure 7B), sensitivity to posture changes (Figure 7E),

246   and righting gain (Figure 7K), all of which contributes positively to their higher posture stability.

247   These results demonstrate that SAMPL is capable of detecting inter-strain variations in locomo-

248   tion and balance behavior.

249   In contrast, larvae of different ages adopt different strategies to stabilize posture and navigate

250   in depth [16–18] To contextualize the magnitude of strain-related differences we gathered a lon-

251   gitudinal dataset by measuring behavior from the same siblings of the AB genotype at three

252   timepoints: 4-6, 7-9, and 14-16 dpf (Table 3). We observed that the standard deviation of IBI

253   pitch for 4 and 14 dpf larvae was 38.1% higher and 11.3% lower, respectively, than the aver-

254   age result of 7 dpf larvae (Table 3). Across strains at 7 dpf, the variation was much smaller: from

255   11.8% higher to 11.2% lower. Similarly, relative to 7 dpf larvae, sensitivity of 4 dpf larvae was

256   considerably lower (-42.5%), and increased to 23.6% higher by 14 dpf (Table 3); variations among

257   7 dpf strains were up to 10.0% lower and 15.4% higher.

258   Our analysis of new data supports three key conclusions. First, SAMPL can uncover small, sys-

259   tematic differences in the way fish swim and stabilize posture. Second, SAMPL can make lon-

260   gitudinal measures of the same complement of animals as they develop. Third, relative to de-

261   velopment, the effect of genetic background is small. We conclude that SAMPL's capacity to

262   resolve small differences supports its usefulness as a tool screen for modifiers of postural con-

263   trol and vertical locomotor strategies.

264   **Estimating SAMPL's resolution**

265   Our dataset establishes SAMPL's ability to resolve small kinematic differences between cohorts.

266   How does SAMPL's power change as a function of the size of the dataset? We used resampling

267   statistics to estimate SAMPL's resolution as a function of the number of the bouts (Methods).

268   To ensure our most conservative estimate, we resampled data combined across AB, SAT and

269   WT genotypes at 7dpf.

270   As expected, the width of the confidence interval for any estimated parameter decreased with

271   the number of bouts (Figure 8A). The most challenging parameter to estimate is coordination

272   between fin and trunk (fin-body ratio) The steepness with which the confidence interval width

273   decreases follows the number of regression coefficients necessary for each measure: fin-body

274   ratio (4 parameters); bout timing (3 parameters); and steering or righting (2 parameters). We

275   therefore propose that these particular measures can serve as a general guide for the chal-

276   lenge of estimating parameters within a SAMPL dataset.

277   A fundamental challenge for all screens is determining the sample size required to correctly

278   reject the null hypothesis[34]. We address this question by asking how much data one would

279   need to gather in order to detect meaningful effects. We simulated difference of particular

280   magnitudes by imposing an offset on each parameter (sensitivity, steering gain, fin-body ra-

281   tio, and righting gain) while preserving the original variance (Methods). Offsets were expressed

282   as a fractional difference, and resampling was used to estimate the effect size one would see

283   as a function of the number of bouts/IBIs when comparing kinematic parameters between the

284   original dataset and the dataset with an imposed effect (Methods).

285   Broadly, we find that for all kinematic parameters, the smaller the percent change, the larger

286   the required sample size (Figure 8B). Steering and righting gains require the fewest bouts to

287   detect a 1-2% change with an effect size > 0.5 (Figure 8B, green and red). However, sensitivity

288   and fin-body ratio require relatively larger datasets to confidently discriminate small changes

289   (Figure 8B, brown and magenta). We conclude that the full "two-week" dataset we generated

290   using SAMPL (n = 121,979 bouts) is sufficient to reveal any biologically-relevant differences be-

291   tween two conditions.

292   In summary, these simulations demonstrate that a single SAMPL rack divided into two condi-

293   tions (6 apparatus / each) could, in two standard 48-hour runs, generate sufficient data to re-

294   solve meaningful differences in postural and locomotor kinematics between two conditions.

295   We provide detailed instructions in Appendix 5 addressing experimental design strategies to

296   maximize SAMPL's resolution.

DISCUSSION

298   We present SAMPL, a scalable solution to measure posture and locomotion in small, freely-

299   moving animals. We start with a brief overview of the hardware and software, with compre-

300   hensive guides to every aspect of SAMPL's hardware and software included in the Appendices.

301   Next we illustrate SAMPL's flexibility with raw video & real-time measurements from three com-

302   mon model organisms: *Drosophila melanogaster* (fly), *Caenorhabtitis elegans* (worms), and

303   *Danio rerio* (zebrafish). To illustrate the depth of insight accessible using SAMPL we explored a

304   new dataset – consisting of two weeks worth of data – that illuminates four key parameters of

305   zebrafish navigation in depth: bout timing, steering, fin-body coordination, and righting. We

306   made two discoveries using SAMPL's analysis suite: (1) systematic changes to zebrafish pos-

307   ture and locomotion across genetic backgrounds and (2) that these changes were small rela-

308   tive to variation across developmental time. Finally, we use our new dataset to define SAMPL's

309   resolution: how much data an experimenter would need to collect to detect meaningful ef-

310   fects. Taken together, SAMPL provides a screen-friendly solution to investigate vertical locomo-

311   tion and/or other behaviors using common small model organisms, and a turn-key solution to

312   study balance in larval zebrafish. More broadly, our approach serves as a template for laborato-

313   ries looking to develop or scale their own hardware/software. Below we detail SAMPL's innova-

314   tions and limitations, and make a case for screens to address unmet clinical needs for balance

315   disorders.

316   **SAMPL's innovations**

317   One of SAMPL's key innovations is to measure vertical behavior, where the effects of gravity

318   play a role. The overwhelming majority of studies monitor animal behavior from above, where

319   animals are constrained to a horizontal plane. For most animals – especially those that swim

320   or fly – vertical navigation and its neuronal representation[35,36] is vital. Further, maintaining

321   posture in the face of gravity is a universal challenge[37–39], particularly as animals develop[16,40].

322   SAMPL can illuminate animal trajectories during exploration of depth.

323   SAMPL reduces the dimensionality of behavior along a number of axes in real-time. First, by

324   focusing on a homogeneous part of the behavioral arena, SAMPL bypasses a number of imag-

325   ing challenges and difficulties involved in interpreting behavior along arena walls[41]. Second, by

326   rejecting frames with multiple animals in view at the same time SAMPL incorporates animal-

327   to-animal variability[4] within each estimated parameter without having to keep track of individ-

328   uals; the narrow chamber (Figure 1E) is ideal for single-animal experiments if such variability

329   is of interest. Third, while large enough to permit unconstrained behavior, the anisotropic di-

330   mensions of SAMPL's behavioral arenas (Figure 1E) facilitate measurements in the vertical axis.

331   SAMPL's design choices thus facilitate rapid extraction of behavioral parameters relevant for

332   posture and locomotion.

333   SAMPL was designed to scale efficiently. Data is gathered by a compiled executable, allowing

334   SAMPL to run three apparatus off a single computer, reducing costs and space. A SAMPL rack

335   consists of 12 apparatus running off four computers with a footprint of 24"x36"x81.5" (LxWxH).

336   The key components such as the camera are readily available from multiple suppliers. Taken

337   together, SAMPL can be used immediately to screen and/or to provide videographic data from

338   freely moving animals at scale.

339   Our new dataset, gathered in two weeks, illustrates the power of SAMPL's analysis/visualization

340   workflow for studies of larval zebrafish balance. While SAMPL can and does save video, by de-

341   sign it extracts only three parameters in time: the (x,z) coordinates of the animal and the angle

342   between the body and the horizon. As we demonstrate here, this small set of parameters de-

343   fines behaviors larval zebrafish use to swim and balance in depth: bout timing (Figure 3), steer-

344   ing (Figure 4), fin-body coordination (Figure 5), and righting (Figure 6). While each parameter

345   has been previously defined [16–18], the new data we present here illustrates differences across

346   genetic backgrounds and development and allows granular estimation of statistical sensitivity.

347   Taken together, SAMPL's focus facilitates exploration of unconstrained vertical behavior.

Comparisons with other approaches

349   Here, we discuss SAMPL's advantages by comparing it with other available tools for measuring

350   *Drosophila*, *C. elegans*, and zebrafish behavior.

SAMPL for measuring *Drosophila* behavior

352   SAMPL offers advantages over previous methods for measuring negative gravitaxis, an innate

353   behavior of *Drosophila melanogaster* [42]. The most widespread method, called the bang test,

354   consists of banging flies down inside a vertical tube and then counting the number of flies

355   that walk an arbitrary vertical distance in an arbitrary amount of time [42–45]. This method star-

356   tles the flies, which may confound the behavior, and the flies are limited in directional choice.

357   Using SAMPL, a measurement of fly vertical position and orientation is instantaneously ac-

358   quired without needing to startle the flies. Another *Drosophila* gravitaxis assay is the geotaxis

359   maze [46], that allows the flies to make a series of up-or-down choices as they move across the

360   maze towards a light. While the flies are not startled in this assay, they are still constrained to

361   moving only up or down. SAMPLs high resolution camera permits continuous monitoring of

362   free vertical walking behavior, as well as high-resolution monitoring of head, wing, leg, and an-

363   tenna positions. While SAMPL has been designed to monitor behavior in the vertical plane, the

364   hardware and software strategies we have developed for high throughput recording could be

365   similarly adapted to increase the throughput of measuring other *Drosophila* behaviors such as

366   grooming [47], sleep [48], courtship [49], and aggression [50]. Because SAMPL has both high resolution

367   recording and the ability to scale, screening through microbehaviors like head tilting or limb

368   positioning is possible. Notably, an earlier version of SAMPL's detection algorithm was success-

369   fully used for data acquisition in a fly olfactory behavior assay [51,52] with minimal changes. Taken

370   together, SAMPL's resolution, throughput, and adaptability complement and extend current

371   approaches to measure *Drosophila* behavior, particularly in the vertical axis.

SAMPL for measuring *C. elegans* behavior

The simple nervous system of *C. elegans* is a powerful model to study neural circuits that control posture and movement. *C. elegans* possess a rich and tractable repertoire of motor control[53]. For example a pattern generator creates sinusoidal waves of muscle contraction that propel *C. elegans* on a solid substrate, and these sinusoidal movements are sculpted by proprioceptive feedback[54]. Proprioceptive feedback also controls transitions between sinusoidal crawling and non-sinusoidal bending that can propel animals in a liquid environment[55–57]. Other sensory stimuli elicit coordinated motor responses that are critical for navigation. Decreasing concentrations of attractive odorants and gustants trigger reversals followed by a pirouette or omega bend, which results in a large-angle turn that reorients animals[58,59]. A distinct navigation behavior involves precise steering of an animal as it follows an isotherm in a temperature gradient[60,61] or tracks a preferred concentration of gustant[62]. The resolution and scalability of SAMPL offers the opportunity to determine the cellular, molecular, and genetic underpinnings of these diverse motor control mechanisms.

C. elegans behavior becomes complex in enriched 3D environments, with animals using strategies for exploration and dispersal not seen under standard laboratory conditions[63]. Behavior trackers that have been used to study *C. elegans* kinematics are generally restricted to analysis of behaviors on a surface. By contrast, SAMPL measures behavior in a volume and is well-suited to the study of newly discovered behaviors that are only expressed in environments that vary across depth. One such example is gravitaxis, where *C. elegans* display both positive[64] and negative gravitaxis[65], underscoring the need for additional pipelines to test behavior[66]. The new data we present here establishes that SAMPL offers a powerful complement to existing pipelines for *C. elegans* assays of behavior in the vertical dimension.

SAMPL for measuring zebrafish behavior

SAMPL joins a decades-long tradition of apparatus that has, collectively, established the larval zebrafish as a key vertebrate model to understand the neural control of posture and locomotion[13–15]. Broadly, these devices sit on a continuum that represents a trade-off between imaging resolution and throughput. At one end, exquisite measures of tail or eye kinematics are available when imaging single animals that are partially restrained[67], or contained in a small field of view[68]. Such devices are particularly useful when combined with imaging or perturbations of neuronal activity, but at the cost of throughput. At the other end are devices that measure activity when single animals are constrained to small arenas, such as the ~8 mm^2

404 wells in a 96-well plate[6,69–71]. These devices lend themselves well to screens, and offer com-

405 mercial options, but the range of behaviors is compressed[72]. Like other attempts to preserve

406 high-resolution kinematic information while accommodating natural unconstrained behav-

407 ior[22,73–78], SAMPL sits between these two extremes, joining other open-source software pack-

408 ages such as Stytra[79] and Zebrazoom[80]. We see SAMPL as a complementary tool. SAMPL's

409 emphasis on vertical behavior and its scalability position it to leverage the advantages of the

410 zebrafish model for screens – either as a primary resource, or to follow-up on promising "hits"

411 identified with higher-throughput approaches[6].

Screening

413 Balance disorders present a profound and largely unmet clinical challenge[19]. Because the

414 neuronal architecture for balance is highly conserved and the fundamental physics (i.e. grav-

415 ity is destabilizing) is universal, animal models represent a promising avenue for discovery. Due

416 to their size, low cost, molecular accessibility, high fecundity, and conserved biology small an-

417 imals – both vertebrates and invertebrates[81] – have long been used in successful screens of

418 both candidate genes[82], peptides[83] and therapeutics[84,85]. Zebrafish are an excellent exem-

419 plar, particularly in the space of neurological disorders[3], with well-established approaches for

420 candidate gene screens[2,5], peptides[86], small molecules[87–91], and disease models[92]. Using

421 SAMPL with zebrafish, our dataset establishes a foundation to screen for balance modifiers in

422 health & disease.

423 One particular arena where zebrafish screens for balance/posture could have a profound im-

424 pact is in addressing the unmet therapeutic need that exists for a neurodegenerative tauopa-

425 thy: progressive supranuclear palsy (PSP). PSP is initially characterized by balance impairments,

426 falls, vertical gaze palsy, and rigidity[93,94]. Falls are central to early[95] PSP presentation and di-

427 agnosis[96,97] and lead to fractures and hospitalization[96,98]. Currently, no treatments improve

428 balance. Studies of posture[99–103], graviception[104], reflexes[105–108], electromyography[109,110],

429 and neural balance circuits in PSP[103,111–115] are often underpowered, inconsistent, and have

430 yet to identify the specific mechanism or substrate causing falls. Like most genes and subcor-

431 tical structures[116–123] the genetic and anatomical substrates of PSP are conserved between

432 humans and zebrafish[124–127]. Here, using SAMPL, we define behavioral endpoints that reflect

433 how pathological zebrafish might "fall." By establishing SAMPL's resolution, our data lay the

434 foundation for impactful discovery in the space of a neurodegenerative disorder with balance

435 pathology.

Future prospects

SAMPL uses low-cost videographic and computing hardware to make novel behavioral mea-
surements. By optimizing scalability, resolution, and extensibility, SAMPL allows experimenters
to rapidly measure unconstrained behavior as animals navigate in depth. We have used SAMPL
with a model vertebrate, zebrafish, to gain insight into posture and vertical locomotion, and to
lay the groundwork for future screens. A wide variety of neurological disorders present with
balance and locomotor symptoms. SAMPL offers a way to both understand the fundamental
biology of balance, as well as means to evaluate candidate therapeutics to address this unmet
need. More broadly, SAMPL stands as an exemplar and resource for laboratories looking to de-
velop, adapt, or scale videographic apparatus to measure behavior in small animals.

Limitations of the study

Any apparatus necessarily reflects a set of trade-offs. Consequentially, each of SAMPL's inno-
vations can reasonably be recast as a limitation depending on experimental priorities. For ex-
ample, SAMPL's focus on a subset of space and parameters is ill-suited to reconstruct a catalog
of behaviors from videographic measurements i.e. a computational ethogram[11,20]. Similarly,
SAMPL assumes that the animal's trajectory reflects coordinated use of its effectors (limbs/trunk/wings).
While SAMPL's videos would be an excellent starting point for markerless pose estimation,
detailing the links between effector kinematics and resultant changes to posture and trajec-
tory may be better served by a multi-camera setup[8,9]. SAMPL's processing is exclusive to one
animal; other approaches are therefore necessary to resolve social interactions[7,128]. Finally,
SAMPL's analysis/visualization toolset incorporates priors for movement of zebrafish only – stud-
ies of other species would require a moderate investment of effort.

ACKNOWLEDGMENTS

Movie 1

Movie 1. Stop motion instruction for box assembly.

Movie 2

Movie 2. Example of recorded epochs of a fly, a shrimp, and a worm. Scale bar: 2 mm.

Movie 3

Movie 3. Top: example of a recorded epoch of a freely-swimming zebrafish larva using the apparatus. Bottom: swim speed and pitch angles plotted as a function of time. Scale bar: 1 mm.

474 **STAR METHODS**

475 **RESOURCE AVAILABILITY**

476 **Lead contact**

477 Further information and requests for resources and reagents should be directed to and will be

478 fulfilled by the lead contact, Dr. David Schoppik (schoppik@gmail.com).

479 **Materials availability**

480 This study did not generate new unique reagents.

481 **Data and code availability**

482 SAMPL source code, SAMPL executables, raw behavior data, analyzed data used to make paper

483 figures and `README.md` descriptions of each are all deposited with the Open Science foundation

484 and are publicly available. DOI is listed in the key resources table. All original code has been

485 deposited at the Open Science foundation and is publicly available. DOI is listed in the key re-

486 sources table. This resource includes code to generate each figure / table in this manuscript.

487 Any additional information required to reanalyze the data reported in this paper is available

488 from the lead contact upon request.

489 **EXPERIMENTAL MODEL AND SUBJECT DETAILS**

490 All procedures involving larval zebrafish (*Danio rerio*) were approved by the New York Univer-

491 sity Langone Health Institutional Animal Care & Use Committee (IACUC). Zebrafish larvae were

492 raised at 28.5°C on a standard 14/10 h light/dark cycle at a density of 20-50 larvae in 25-40

493 ml of E3 medium before 5 days post-fertilization (dpf). Subsequently, larvae were maintained

494 at densities under 20 larvae per 10 cm petri dish and were fed cultured rotifers (Reed Mari-

495 culture) daily. Larvae that had their behavior measured at 14 dpf were raised as stated above

496 before being moved to 2 L tanks with 300 ml of cultured rotifers at 9 dpf. At 13 dpf, they were

497 transferred back to petri dishes with E3 medium for adaptation.

498 Larvae with different strains were achieved by crossing Schoppik lab strain with a mixed AB, TU,

499 and WIK background to three different wild-type strains: AB (Zebrafish International Resource

500 Center), mixed background of AB/WIK/TU, or SAT (Zebrafish International Resource Center).

501 Reference parameter values in Table 3 for 4, 7, 14 dpf fish were gathered using the AB strain

502 fish.

503 *Drosophila melanogaster* (w^{1118}) were raised at 23°on standard cornmeal-agar food under a

504 12/12 light/dark cycle.

505 *Caenorhabditis elegans* (*C. elegans*) were grown at 20°on nematode growth medium agar

506 plates seeded with *Escherichia coli* OP50 as previously described [129].

METHOD DETAILS

Behavior experiment

509 Larvae at desired age (4, 7, or 14 dpf) were transferred from petri dishes to behavior chambers

510 at densities of 5-8 per standard chamber and 2-3 per narrow chamber with 25-30/10-15 ml

511 of E3, respectively. After 24 h, behavior recording was paused for 30-60 minutes for feeding

512 where 1-2 ml of rotifer culture was added to each chamber. Larvae were removed from the ap-

513 paratus 48 h after the start of the recording.

514 Behavior measurement in this manuscript were collected from 27 clutches of zebrafish larvae

515 between 7 to 9 dpf under constant darkness. 4 dpf and 14 dpf reference parameter values in

516 Table 3 were collected from 10 clutches of zebrafish larvae under constant darkness. Finless

517 data was generated using 4 clutches of larvae under constant darkness. For all experiments, a

518 single clutch of larvae produces one experimental repeat with at least 3 behavior boxes each

519 containing 5-8 larvae per standard chamber or 2-3 fish per narrow chamber.

520 For *Drosophila* recording, four flies were transferred to a narrow chamber. A small piece of

521 water-dampened kimwipe was put at the bottom of the chamber to maintain humidity. A n

522 acrylic plug was secured at the top to prevent them from escaping the chamber. We secured

523 the chamber with the flies in the SAMPL apparatus and performed the standard SAMPL exper-

524 iment using recording parameters provided in Table 2.

525 To image swimming *C. elegans*, eight starved N2 adult hermaphrodites were transferred to a

526 narrow chamber filled with 15 ml M9 buffer (3 g/l KH_2PO_4; 6 g/l Na_2HPO_4; 0.5 g/l NaCl; 1 g/l

527 NH_4Cl) which was secured in the SAMPL apparatus as described above. Behavior recording

528 was started immediately afterwards. Refer to Table 2 for SAMPL thresholds for *C. elegans* de-

529 tection.

Fin amputation

531 6 dpf zebrafish larvae were anesthetized in 0.02% tricaine methanesulfonate (Syndel) and

532 transferred to 3% Methylcellulose (Sigma). Fin amputation was done by removing pectoral

533 fins using fine forceps (FST). Specifically, one pair of forceps was used to stabilize the head of

534 the fish and a second pair was used to grab the joint and pull off the fins. Finless larvae were

535 washed three-times in E3 and fed with cultured rotifers before behavior assessment at 7 dpf.

Video acquisition

Movie 1 was captured using Sigma fp digital camera (Sigma Co.). Video footage was edited and annotated using Premiere Pro (Adobe). Movies 2 & 3 was captured with the innate video capture function in SAMPL software using recording parameters described in Table 2. Movie 3 was edited using Adobe Premiere Pro (Adobe) to combine with timeseries data.

QUANTIFICATION AND STATISTICAL ANALYSIS

Behavior analysis

Behavior data was analyzed using the Python analysis pipeline `SAMPL_analysis_visualization`. `SAMPL_analysis()` function was used to calculate swim parameters, extract bouts and inter-bout intervals (IBIs) from the raw data, and align swim bouts by the time of the peak speed.

Each run of the experiment (recording from "start" to "stop") generates one data file (∗`.dlm`) containing recorded raw parameters including time stamp, fish body coordinates, fish head co-ordinates, pitch angle, epoch number and fish length at every time point. An epoch is defined by a duration where the number of detected pixels falls within the lower and upper threshold for recording, indicating detection of fish in the field of view.

To extract bouts from the raw data, first, swim features, such as speed, distance, trajectory, an-gular velocity, etc., were calculated using basic parameters and time interval. Next, epochs that were longer than 2.5 s, contain maximum swim speed greater than 5 mm/s, and pass various quality-control filters were selected for bout extraction. Epochs containing multiple bouts were segmented and truncated so that each detected bout contains data from 500 ms before to 300 ms after the time of the peak speed. Then, bouts containing 800 ms of swim data were aligned by the time of the peak speed and saved for further analysis.

All further quantification was performed on data during zeitgeber day, namely the 14 h light time for fish raising under 14/10 h light/dark cycle.

To calculate IBIs, epochs with multiple bouts are selected and the duration of swim speed be-low the 5 mm/s threshold between two consecutive bouts is calculated. A 100 ms buffer win-dow is then deducted from each end of the duration to account for errors of swim detection (Figure 3A). Pitch angles during each IBI were averaged to generate an IBI pitch (Figure 3B).

Definition of other bout parameters can be found in Table 3. All bout parameters (except for ki-netic parameters explained in the next section) reported in the main text and Table 3 are mean values across swim bouts collected from multiple experimental repeats. One experimental re-

567 peat is defined as behavior data collected from one clutch of fish over 48 h using at least three

568 boxes.

Computation of kinetic parameters

570 To calculate larvae sensitivity to pitch changes (Figure 3), we plotted bout frequency as a func-

571 tion of IBI pitch. The data was modeled using a quadratic polynomial regression (least squares)

572 defined by function:

$$y = a(x - b)^2 + c$$

573 where the coefficient of the quadratic term a indicates sensitivity and the y-intersect c repre-

574 sents baseline bout rate.

575 To calculate steering gain (Figure 4), we first computed bout trajectory defined by the tangen-

576 tial angle of instantaneous trajectory. Pitch angles at time of peak speed were then plotted as

577 a function of bout trajectories and modeled with linear regression (least squares). The slope of

578 the best fitted line was termed the "steering gain."

579 Time of peak angular velocity in Figure 5 was computed using adjusted angular velocity. First,

580 pitch angles for each bout were smoothed by a window of 11 frames and used for calculate

581 angular velocity. Next, we flipped the signs of angular velocity for bouts that started with nose-

582 down rotation so that all bouts started with positive angular velocity. To calculate time of peak

583 angular velocity, we took the median angular velocity at every time point across all bouts from

584 the same experimental repeat and found the time for the peak. Peak angular velocity times

585 across all experimental repeats were then averaged to generate mean peak time.

586 For fin-body coordination analysis (Figure 5), we selected swim bout that are faster than or

587 equal to 7 mm/s. Bouts with steering rotations (posture change from -250 ms to 0 ms) greater

588 than the 50th percentile while having a negative attack angle were further excluded from anal-

589 ysis. To calculate fin-body ratio, we plotted attack angles as a function of early rotation. Attack

590 angle is defined as the difference between bout trajectory and pitch at time of peak speed.

591 Body change related to steering were calculated by subtracting pitch angles at time of max

592 angular velocity by initial pitch. Attack angle-rotation plot was then fitted with a logistic func-

593 tion defined by

$$y = a + \frac{h}{1 + e^{-k(x+b)}}$$

594 where h is the height of the sigmoid. Fin-body ratio was defined by the maximal slope esti-

595 mated using $kh/4$.

596   To calculate righting gain and set point (Figure 6), righting rotation, defined by the pitch

597   changes from time of peak speed to 100 ms after peak speed, was plotted as a function of ini-

598   tial posture. Righting gain was determined by the absolute value of the slope of the best fitted

599   line. The x intersect of the fitted line determines the set point (Figure 6E, blue cross) indicating

600   posture at which results in no righting rotation.

601   **Estimating effects of sample size on statistical modeling of bout kinetics**

602   For statistical analysis of swim kinetics (Figure 8A), the 7 dpf constant dark behavior dataset

603   was sampled for 20 times at given sample number for calculation of swim kinetics and CI

604   width. Specifically, sensitivity is determined by the coefficient of the quadratic term of the fit-

605   ted bout-timing parabola as stated above. To plot estimated error as a function of the number

606   of IBI, sets of data with N number of IBIs were sampled from the 7 dpf constant dark behavior

607   dataset. However, different from the calculation of R^2 above, the total dataset was sampled for

608   20 times for each desired number of IBIs (N). Regression analysis was performed on each set of

609   sampled data to calculate sensitivity and its standard error. Estimated errors were used to cal-

610   culate CI width at 0.95 significance level using normal distribution for each sampled dataset.

611   Similarly, steering gain and righting gain and their estimated errors were calculated from N

612   number of bouts sampled from the original dataset. Estimated error was used to calculate CI

613   width at 0.95 significance level for each sampled dataset. Sampling at each N was repeated for

614   20 times to generate error bars on the CI widths.

615   Fin-body ratio was calculated from N number of bouts sampled from the original dataset and

616   repeated 20 times for each N. Because fin-body ratio is determined as the maximal slope of

617   the sigmoid which is given by $kh/4$, the variance of fin-body ratio (slope) is calculated using for-

618   mulation

$$V_{slope} = (E_k^2 \times V_h + E_h^2 \times V_k + V_k \times V_h) \times (1/4)^2$$

619   where E_k and E_h are the mean of k and h with V_k and V_h being their respective variance. Next,

620   the standard errors of the fin-body ratio were calculated and used to estimate CI widths at 0.95

621   significance level.

622   To estimate effect sizes at given percentage of change (Figure 8B), an artificial data set was

623   generated by altering the coefficient of interest while maintaining other coefficient as well as

624   y residuals at given x values. N data points were drawn with replacement from each data set for

625   calculation of kinematic parameters, which was repeated 200 times to generate distributions

626   of parameters of interest. Effect sizes were determined using Cohen's d:

$$ES = \frac{|\mu_{sim} - \mu_{ori}|}{\sigma}$$

627   where μ_{sim} and μ_{ori} are the mean of parameter values calculated from respective data sets

628   and σ is the standard deviation of all 400 calculated parameters. The whole process was re-

629   peated for 20 times to estimate the mean effect size at given sample size (N) and percent-

630   age of change. To reduce program execution time, we used a fixed 40 ms before time of peak

631   speed as the time of max angular velocity for fin-body ratio calculation. Other kinematic pa-

632   rameters were calculated as described above.

APPENDIX 1: HARDWARE DESIGN PRINCIPLES

Camera

At the time of writing, the best price/performance ratio when using infrared light are the Sony Exmor line of complementary metal-oxide-semiconductor (CMOS) sensors. Sensors in the Exmor line are usually released as pairs, with a low-cost low-speed version of the same sensor available at the same time as a more expensive high-speed version. Our initial designed used the lower-cost IMX249 sensor; we have since switched to the faster IMX174 variant. These two sensors have a particularly large pixel size (5.86um), low noise (7e-), and a large well depth (32,513e-) allowing for exceptional dynamic range (73dB) and signal-to-noise ratio (45dB) at high-definition resolution (1936x1216 pixels). Quantum efficiency >900nm (i.e. the infrared range we will use) is 10%. Sony has released new sensors in the Exmor line regularly, but the trend has been to release sensors with increasingly small pixels. Thus for our purposes, the performance of the IMX174 remains unmatched.

Machine vision cameras are available with different interfaces used to stream data to a computer. The major difference between interfaces is the bandwidth available to each. The two most common interfaces for machine vision cameras at the time of writing are Gigabit Ethernet (125MB/sec) and USB3.0 (500MB/sec after overhead). Currently, there are commercially-available cameras with higher bandwidth interfaces utilize 10-tap CameraLink (850MB/sec), 10 Gigabit Ethernet (1250 MB/sec), 4xCoaXPress 2.0 (6,250MB/sec), and PCIe x8 (7,000MB/sec). Running our preferred IMX174 sensor at full resolution and speed for 8-bit images only requires 380MB/sec. Thus, USB3.0's low cost and relative ubiquity made it the most attractive option for our apparatus.

There are a number of manufacturers that make cameras built around the IMX174 with a USB3.0 interface. Cameras from major manufacturers all conform to the GenICam standard making them largely interchangeable, particularly when using the Vision Acquisition software from National Instruments. We have successfully used cameras from Ximea (MC023MG-SY), Basler (acA1920-155um), and FLIR (GS3-U3-23S6M-C), others include SYSVistek (exo174CU3) and Daheng Imaging (MER2-230-168U3M). We have also used cameras ordered directly from different manufacturers – at a substantial discount – available via alibaba.com: Hangzhou Huicui Intelligent Technology Co. Ltd. (A7200MU130), Hangzhou Contrastech Co. Ltd. (Mars2300S-160um), Shenzhen Hifly Technology Co. Ltd. (MV-AU231GM). When ordering directly from manufacturers we specify Delivery At Place (DAP) shipping.

665 The primary differences that we've encountered are whether a particular model implements

666 binning or other on-camera computations, heat management, and different manufacturer-

667 provided APIs. When we use multiple cameras from the same manufacturer on the same

668 computer, we have also noticed that certain cameras will throw timeout errors on some USB

669 ports but not others; shuffling cameras and ports has worked to solve this problem. At the

670 time of writing, supply chain issues mean that most major camera companies quote long lead

671 times, but cameras ordered directly through alibaba.com all shipped within two weeks.

672 **Illumination**

673 Image quality is proportional to available light. Further, the size of the illuminated area defines

674 the size of the field that can be imaged. Finally it is imperative for our experiments that from

675 the fish's perspective that the "dark" period is completely dark. We therefore chose 940nm

676 LEDs as our source of infrared illumination. This left us with three options to build our illumina-

677 tion source: LEDs mounted on adhesive strips, "star" style LEDs with 1-4 dies on a single PCB,

678 and a high-power LED array. The LED strips had too little illuminance for our purposes due pri-

679 marily to the spacing of the LEDs. The high-power LED array had ample illuminance but gen-

680 erated so much heat that it required active cooling.

681 We developed a simple illumination module to provide diffuse IR light across a 50mm circle

682 An LED mounted on a "star" PCB (Opulent LST-01F09-IR04-00, Mouser) provided ample light.

683 We mount each "star" LED with thermal adhesive to a small heat sink (Ohmite SV-LED-325E)

684 which in turn is glued to a Thorlabs adapter (SM1A6FW) to allows the wires to exit and the

685 LED/heatsink to connect to collimation and diffusion optics. The heat sink is machined (either

686 with a Dremel hand-held tool or a mill) on one side to allow the wires that power the LED to lie

687 flat against the heatsink. We power multiple illumination modules in series using a constant

688 current LED driver (LuxDrive BuckBlock 1000mA). Our illumination setup generates negligible

689 heat and our modules run continuously for years.

690 Our imaging parameters are fixed across experiments and optimized to give the highest qual-

691 ity data we can achieve with our hardware. The gain of the camera is set either to its lowest

692 value or just above to minimize noise. Our exposure time is either 750 μsec or 1msec, allowing

693 for a crisp image in the face of the fastest movements that fish can make. The illuminated area

694 is circular, but the image sensor size is rectangular. We therefore crop the sides of the image to

695 produce a square that fits within the illuminated area.

Lens

Our choice of lens was guided by the need to balance different demands:

1. The longer the working distance, the greater the space needed between the sample and the lens. We wanted our apparatus to fit length-wise on a 24 inch shelf, and so we needed to minimize the working distance.

2. The entire depth of the tank needs to be in focus, but not beyond that because we'd like to blur our LED.

3. The lens should be coated to pass IR light

4. The lens should be easy to mount to the base of the apparatus; mounting the lens instead of the camera allows drop-in replacement of cameras from different manufacturers, which have different positions of the tripod mount relative to the sensor.

5. The lens should have a simple way to mount an IR-pass filter (e.g. common thread).

Unfortunately, we were not able to find a single lens that met all of these criteria. Instead, we adapted a 50mm (Edmund Optics 67717) lens by placing a small Thorlabs tube (ThorLabs SM1-L03) between the lens and the camera. We mounted a 25mm IR pass filter (ThorLabs FGL830) inside the Thorlabs tube. By moving the lens farther from the sensor we decreased the minimum working distance sufficiently. Finally, the Thorlabs tube allows us to mount the lens to the breadboard directly.

Behavioral arena

To maximize the amount of time the fish swam in a plane orthogonal to the camera, we used rectangular chambers. Initially we chose glass colorimeter cuvettes (Starna Cells Inc, Atascadero CA): they are made of an inert material (glass) and come in a variety of sizes. Due to supply chain issues, we switched to custom-fabricated chambers, plans attached. We now assemble these from laser-cut acrylic, cementing a front and back side to a u-shaped piece that forms the other sides. These chambers are considerably cheaper and less prone to breakage than glass and can be rapidly modified to allow for different experiments.

Enclosure

We designed a custom aluminum base with tapped holes for post-holders for the IR LED, chamber holder, and camera/lens/filter holder. We used custom-cut extruded aluminum rails to frame the sides and top. The sides are made of black foam-core sized to fit in grooves in the breadboard and rails. The top rails have a cross piece that holds the LED strip used to provide

727   circadian lighting. All parts are fabricated to order by Base Lab Tools Inc (Stroudsburg PA). The

728   top is a steel tray fabricated to order by MetalsCut4U (Avon Lake OH). Our current enclosure

729   took roughly three months to prototype before settling on the final design.

Shelving and fleet organization

731   We have organized our fleet of apparatus to sit on mobile wire shelving. Currently, we use

732   36"x24"x81.5" adjustable wire shelving units (McMaster Carr, Robbinsville NJ). We prefer to

733   have the shelving on casters as it makes accessing the back of the units considerably easier.

734   Shelving is organized such that one computer and three apparatus sit on a single shelf. En-

735   closures on a given shelf are color-coded (blue, gold, and red) so that each apparatus can be

736   uniquely identified by a color/shelf/module combination; this also facilitates wire labeling. Each

737   shelf has its own power strip that controls the computer, the IR lights, and the white LEDs; all

738   strips plug into a single uninterruptible power supply (APC SmartUPS 1000C).

739   Our aim in specifying module size was to ensure that multiple investigators could set up ex-

740   periments simultaneously, and to minimize the cost One unit has four shelves so that a sin-

741   gle "module" consists of four computers and twelve apparatus. Each module has a dedicated

742   monitor/keyboard/mouse on an adjacent desk, shared by the four computers using a KVM

743   switch (IOGEAR GCS1794). A module has its own dedicated unmanaged Ethernet switch

744   (NETGEAR GS110MX) that allows Gigabit speed communication between computers and 10

745   Gigabit speed between modules.

Computer hardware

747   Computer hardware was chosen to ensure adequate performance while minimizing cost,

748   noise, and size. We found that building our own computers was the only path forward in the

749   face of supply chain issues and strict optimization criteria. We opted to build around what

750   was, at the time of writing, the previous generation of AMD microprocessors (Ryzen 7 5700G)

751   cooled by a Noctua NH-L9a-AM4 fan (to minimize acoustic noise). We chose a Mini-ITX form

752   factor motherboard that allowed us to use a small case (Cooler Master NR200). Other parts

753   (64GB RAM, SSD, power supply) were chosen based on availability; a full parts list is attached

754   (Table 1). We recommend using https://www.pcpartpicker.com to minimize cost and ensure

755   compatibility of different components. All computers run Windows 10 Professional (Microsoft,

756   Redmond WA).

APPENDIX 2: ACQUISITION SOFTWARE DESIGN PRINCIPLES

What we don't measure

To extract the maximum amount of useful information about posture and locomotion with the minimum amount of overhead we had to be selective about what we measure. Our imaging field is located in the center of the arena; fish that swim at the bottom, top, or sides of the tank where there is a boundary are excluded from tracking. While multiple fish swim in the same arena, we do not take data when more than one fish is in the imaging field to sidestep the need to track fish identity. Our arena is sized to allow fish to swim freely but its shape (a rectangular solid) encourages fish to swim in line with the imaging plane; we exclude frames where fish turn away from the field of view (i.e. are swimming towards/away from the camera). Finally, capturing the full range of rapid propulsive undulations of the fish tail requires a frame rate of 500Hz-1kHz[130,131]. As changes to posture and locomotion are much slower, we opted to record at 160Hz. Together, these choices allowed us to optimize our algorithms to achieve the speed necessary to process video in real-time.

Algorithms to measure posture and position

Our apparatus extracts the position and pitch orientation of zebrafish in real-time over days using a simple set of common machine vision processing steps:

1. Measure the absolute difference between the current frame and the background (fish-free) image.
2. Threshold the difference image such that all small differences are set to zero.
3. Dilate the image three times in succession to remove any larger clumps that are still smaller than a fish.
4. Extract and quantify all particles in the image.

Real-time video processing allows efficient data extraction during video acquisition. Our design of the architecture is further discussed in the section: Optimizations for speed.

Below we detail a number of additional processing and optimization steps to ensure that we maximize useful data.

Measuring the pitch of the fish

To extract the pitch (the angle of the fish with respect to the horizon), we perform the following steps to ensure that the sign and magnitude of the angle is correctly assigned:

1. Fit the particle with an ellipse and extract the angle of the long axis with respect to the horizon.

789   2. Threshold the original difference image again to identify the pixels that correspond to the
790   head of the fish.

791   3. Using the head and body (X,Y) coordinates determine whether the fish was facing to the left
792   or right.

793   4. Assign the correct angle and sign such that nose-up posture is always positive and nose-
794   down is always negative.

795   These steps ensure that the data saved follows a simple and intuitive convention for posture.

Optimizations for speed

797   To optimize our code for speed, we use a set of thresholds to rapidly evaluate and reject frames

798   1. Before any processing, we sum the pixel values in the frame. If it is too low (no fish in frame)
799   or too high (more than one fish in the frame) we reject the frame.

800   2. After the particles are identified we reject the frame if a particle is touching the edge (fish
801   partially out of frame), if there is more than one particle (multiple fish) or if the length of the
802   particle is too short (fish bending in/out of the field of view). We define an epoch as a set of
803   continuous frames that pass all our exclusion criteria (i.e. that contain a single fish in frame).
804   Epoch duration is tracked and, when too short, can be rejected.

805   In addition to optimizing the algorithm, we adopted a producer-consumer architecture to de-
806   couple video acquisition from video processing and saving data. Our software runs two rou-
807   tines: the "producer," which acquires frames from the camera and places them in a queue
808   in memory, and the "consumer" that extracts each frame from the queue and processes it in
809   turn. Our program monitors the size of the consumer buffer and, if it has less that 10% free,
810   pauses the producer routine for 15 seconds to allow the buffer to clear. In this configuration,
811   the performance ceiling shifts from CPU speed (i.e. how quickly can a frame be processed) to
812   the amount of RAM available (i.e. how many frames can be queued). At the time of writing this,
813   doubling the amount of RAM is considerably less expensive than doubling CPU performance.
814   The choice of architecture thus brings down the cost of the computer.

Saving raw video

816   While the bulk of our experiments rely on real-time processing of video it is often useful to save
817   the actual data. Further, we wanted to be able to set user-defined criteria to determine in real-
818   time which videos were worth saving. Leveraging the producer-consumer architecture, our
819   software contains a routine that independently buffers the frames being analyzed and, if, the
820   video to be saved meets user-defined criteria, will pass the frames to an independent program

821 to write them to disk. For example, we can ensure that the video to be saved is of a certain

822 length. Similarly, we can filter the video images[132] to determine if the target is in crisp focus

823 (useful for larger arenas, or higher magnification) and only save high quality videos. By separat-

824 ing video writing from acquisition and processing, comparatively slow operations such as video

825 compression and/or saving video to a network-accessible shared drive do not compromise per-

826 formance.

Apparatus control software

828 Our algorithm relies on common and mature image processing routines and could be instan-

829 tiated in any modern programming language. Since we had run this algorithm for the better

830 part of a decade we were confident that it was sufficiently stable to compile into a distributed

831 executable, which would greatly simplify deployment to a fleet of apparatus. Our original im-

832 plementation was written in LabVIEW (National Instruments, Austin TX) which was stable and

833 accommodated all the lab's hardware changes for the past decade. We therefore opted to up-

834 date the LabVIEW code, which we distribute both as source and executable versions. Running

835 the executable requires each computer to have the LabVIEW Runtime Engine (free download)

836 installed, as well as a license for NI Vision Acquisition software (NI 778413-35) and the Vision

837 Development Module Run-Time engine (NI 778044-35).

User interface

839 We designed the interface to enable easy initialization of experiments, rapid graphical and

840 quantitative visualization of video processing and performance, and to minimize error. Launch-

841 ing the executable starts the program, which allows the user to fill out various text, numeric,

842 and drop-down fields that describe the experiment. The user then monitors the video feed un-

843 til no fish are in frame and then selects that image as the background. We have found that this

844 initial bit of monitoring both compensates for slight day-to-day differences in arena placement.

845 More importantly, it forces the user to monitor the live feed at the beginning of each experi-

846 ment, a useful bit of mindfulness that minimizes lost data. Once running, the user can: mon-

847 itor the output of each step in the processing algorithm graphically, monitor the number of

848 times the consumer buffer has overflowed (usually zero), update the text fields, and stop the

849 program. Hardware parameters are stored in a text file that can be easily edited directly. Experi-

850 ment parameters are similarly saved to text files and can be reloaded to save time.

851 We have implemented a number of user interface items to minimize confusion in the face of a

852 fleet of instruments. First, we have color-coded versions of the executable (blue, gold, and red)

853 where the background clearly differentiates the version. Each version has its own configura-

854 tion file that, during setup, is coded to a particular apparatus. Thus the user is always aware of

855 which apparatus they are interfacing with based on color cues. Next, we added a "debug" but-

856 ton to the front panel that allows for direct monitoring and editing of all program variables. In

857 "debug" mode the user has the option to save raw video.

858 APPENDIX 3: HARDWARE ASSEMBLY GUIDE

859 In this Appendix, we walk through box assembly and recording settings. Refer to Appendix 5

860 for executing experiments and SAMPL data analysis.

861 Hardware assembly

862 Our design of hardware allows connecting up to three SAMPL boxes to one computer while

863 using one set of power supplies (for IR LED and daylight LED). See Movie 1 for video instruction

864 on box assembly.

865 1. Camera module

866   (a) Attach 1x 1.5 inch post (TR1.5) to the camera module holder (SM1RC). Screw in tightly.

867   (b) Assemble lens and camber. Sequentially connect parts below: camera lens, SM1A10

868   adapter, IR filter, SM1-L03 extension tube, assembled camera module holder, SM1A9

869   adapter, and the camera.

870 2. IR illumination module

871   (a) Attach wired IR LED to the heatsink and SM1A6FW adaptor (see below for instruction).

872   (b) Carefully mount the condenser into SM2L05 tube.

873   (c) Assemble the IR module by sequentially connecting parts below: IR kit, SM1M10 tube,

874   SM1A2 adapter, SM2L20 tube, and the mounted condenser.

875   (d) Tightly attach TR1 post to SM2RC holder.

876 3. Chamber holders

877   (a) Take off rubber covers on the tip of the screws on the chamber holders (FP01).

878   (b) Mount holders onto TR1 posts using 8-32 screws.

879   (c) Assemble the IR module by sequentially connecting parts below: IR kit, SM1M10 tube,

880   SM1A2 adapter, SM2L20 tube, and the mounted condenser.

881   (d) Tightly attach TR1 post to SM2RC holder.

882 4. Put together the box

883   (a) Mount one of the short rails between two long rails using right angle brackets and T-
884   nuts.

885   (b) Mount the other two short rails onto the long rails using slotted cubes and low-profile
886   cap screws (SH25LP38).

887   (c) Adjust the position of the middle rail so that is approximately 13 cm away from one end
888   of the frame.

889   (d) Attach post holders to the base plate using cap screws (SH25S038). Note that the one
890   for the camera module is the longer post holder (PH1.5).

891   (e) Mount 4 medium rails onto the base plate using standard cap screws.

892   (f) Insert all the modules onto the base plate. Connect USB cable to the camera.

893   (g) Make a notch in the middle of the shorter side of a small panel and insert it between
894   the rails on the side of the camera module.

895   (h) Insert 2 large side panels.

896   (i) Attach daylight LED to the top frame (see below for instruction).

897   (j) Pass IR and daylight LED wires through the front notch of the baseplate.

898   (k) Insert the front panel.

899   (l) Attach the top frame.

IR light wiring

901 Solder 2x 9" wires onto the IR LED "star." Attach IR LEDs to heatsinks using HexaTherm tape.
902 Note that in order to pass the wires through the heatsinks and the SM1A6FW adapter on the
903 opposite end, the ears of the Ohmite heatsink need to be trimmed down a little. When done,
904 attach the heatsink to the adapter using thermal epoxy. To simplify light wiring, we use one
905 1000 mA BuckBlock to dirve 3 IR lights in series for 3 boxes on the same level of the shelf. To
906 do this, one needs 2x 7" wires to connect adjacent IR cables and 1x 22" wire connecting the
907 further IR to the BuckBlock. Use another 8" wire to connect the closest IR to the BuckBlock.
908 We recommend using XT60H connectos to link these wires to the IR light cables and connect
909 wires to the BuckBlock for the ease of troubleshooting and replacement. Finally, connect the
910 BuckBlock to 12 V 2 A power supply through pigtail adaptors.

Daylight wiring

912 Each box uses a strip of 6 daylight LEDs. Our choice of daylight LED comes with double sided
913 tape already attached to the back side of the LED which is used to install LED strips to the top

914 frame. To wire daylight LED strips, solder 2x 20" wires to the LED strip. Heat shrink sleeves can
915 be used here to strengthen connections. Twist the wires at the end close to the LED. This helps
916 with cable management in the box. Bend the cables 90 degrees in the XY plane (perpendicu-
917 lar to the illumination direction) so that the wires won't get into the field of view.

918 To simplify light wiring, we use one 12V 1A power supply to drive 3 LED strips in parallel. To do
919 this, cut 1x 27" wire for connecting the positive end of the DC plug to the LED strip. Prepare
920 3 wires for the negative end of the strips each measured 10", 18", and 27". Insert one end of
921 all three wires for the negative end into the negative terminal of a pigtail connector, connect
922 the other ends to the LED cables. For positive end, we recommend using T tap connectors
923 (B085XGYW1B) which allows easy disconnection.

PC setup

925 Assemble computer parts. Make sure 1 PCI-e USB card is installed into each PC. Connect
926 power cable and Ethernet cable. If desired, connect 3 cameras to three different USB BUS on
927 the PC: specifically, one to a PCI-e USB card, one to a USB 3.0/3.1 port on the motherboard in
928 the back of the PC, and one to a USB 3.0 port on the front panel. If desired, connect to the KVM
929 switch.

930 Turn on the PC, setup Windows. If necessary, change settings below to achieve peak perfor-
931 mance: select AMD High Performance in Power Settings; set Sleep time to Never; set hard disk
932 sleep time to 0 in Advanced Power Settings.

Install behavior programs

934 We provide three executable programs (Blue, Gold, Red) that can run simultaneously on the
935 same PC. Refer to the Key Resources Table for access to the programs. To install executables,
936 download `*.exe` files and corresponding configuration files (`* Configuration.ini`). Create a
937 folder under `C:/` and move configuration files to `C:/Data/`. Install required NI software and ac-
938 tivate: LabVIEW Runtime, Vision Acquisition, and Vision Runtime. Restart computer.

939 Open NI Max, rename cameras to `camBlue`, `camGold`, and `camRed`. Set camera settings:

940 · Field of view - X: left = 360; resolution = 1216
941 · Field of view - Y: top = 0; resolution = 1200
942 · Under Acquisition attributes - Receive time stamp mode = System time
943 · Under Camera attributes - Analog control - Gain = 1; Black level = 1 (if applicable)
944 · Under Acquisition Control - Exposure time = 1000; Trigger activation = Rising edge; Frame
945   Rate = Freerun (for 166 Hz with our cameras of choice, or set to desired frame rate)

946 Open configuration files and set box number to desired values. We use box number as a

947 unique identifier for different behavior boxes. Check camera name to make sure it's the same

948 as the corresponding camera names in NI Max.

949 Open behavior programs, now that you should see images showing up on the preview win-

950 dows.

Camera calibration

952 Once the apparatus has been assembled and software has been installed, align the field of

953 view (FOV) to the center of the IR light circle. Raise or lower the post holding the camera mod-

954 ule to center the FOV in Y and roll the module to level it.

955 Next, calibrate the scale of the FOV to 60 pixels/mm. To do this, secure a micrometer in a

956 chamber and place it into the box. Snap a picture of it using NI Max, then measure the scale

957 using the image of the micrometer. If necessary, loosen the SM2RC adapter and move the

958 camera and lens forward or backward to achieve the correct scale.

959 Illumination adjustments should be completed with the behavioral arena in place. To calibrate

960 exposure, first ensure the correct IR light is in use and set the aperture ring between f/16. In

961 NI Max, the peak of the image histogram peak should be around 128 (the middle of the 8-bit

962 range). If necessary, exposure can be reduced by lowering exposure time or increased by open-

963 ing up aperture to f/11.

Network setup

965 We use a Synology data server as a repository to store behavior data. Hard drives are setup

966 as RAID 10. Each SAMPL rack has its own ethernet switch, which can be connected to other

967 switches as necessary.

APPENDIX 4: DATA ANALYSIS SOFTWARE

969 In this appendix, we discuss algorithms for the data analysis and plotting software. We assume

970 that the user is working with data from larval zebrafish here. If not, the specific parameters

971 identified here are unlikely to translate as other organisms move differently but can nonethe-

972 less be used as a starting point. Refer to Appendix 5 for instruction for use. Refer to the Key Re-

973 sources Table for access to the code.

Read DLM files

975 Each SAMPL session (from `Start experiment` to `Stop`) generates one tab-delimited (i.e. `.dlm`) file.

976 Each time point appears as a row of tab-separated values in the `.dlm` file. Columns, from left to

977 right, are time stamp, fish number in the field of view (FOV), pitch angle (0-90°), x coordinate

978 for body, y coordinate for body, x coordinate for fish head, y coordinate for fish head, raw fish

979 angle (0-180°), epoch number, and estimated fish length.

980 Each `.dlm`'s data is loaded as a Pandas DataFrame for further analysis (see

981 `src/SAMPL_analysis/preprocessing/read_dlm.py` for details). Each raw DataFrame contains

982 multiple epochs. An epoch is defined as duration when a fish is detected in the FOV. See

983 Appendix 1 for details on the algorithm for animal detection.

Extract epochs

985 We calculated swim attributes, such as angular velocity, swim speed, instantaneous displace-

986 ment, etc., from recorded pitch angles and fish body coordinates. To extract quality epochs

987 from the recorded data, epochs are analyzed and passed through several quality control filters:

988 1. each epoch is truncated by 50 ms at both the start and the end to eliminate frames when

989   fish is entering/exiting the FOV;

990 2. epochs with duration shorter than 2.5 s are excluded (for 1 & 2, see function `raw_filter()`);

991 3. epochs with frame drop greater than 3 frames are excluded;

992 4. epochs with direction of fish translocation opposite to where the head points toward are

993   dropped (for 3 & 4, see function `dur_y_x_filter()`);

994 5. epochs with aberrant displacement jumps are excluded;

995 6. epochs with improbably large angular velocity greater than 250°/s or angular acceleration

996   larger than 32000°/s^2 are excluded (for 5 & 6, see function `displ_dist_vel_filter()`).

997 All the processes above can be found in the script `src/SAMPL_analysis/preprocessing/analyze_dlm_v4.py`.

Get bout and inter-bout data

999 Epochs that pass the quality control are used to extract swim bouts using function

1000 `grab_fish_angle()` under `src/SAMPL_analysis/bout_`

1001 `analysis/grab_fish_angle_v4.py`.

1002 We use a swim speed threshold of 5 mm/s to determine swim windows. Adjacent swim win-

1003 dows with intervals smaller than 100 ms are combined. Next, we find the time of the peak

1004 speed for each swim window and extract frames in a range of 500 ms before to 300 ms af-

1005 ter that. Inter-bout intervals (IBI) are determined as time between adjacent swim bouts with

1006 a 100 ms buffer window deducted from both the beginning and the end and IBI data is ex-

1007 tracted accordingly. Baseline is considered the time during which larvae swim slower than 2

1008 mm/s and baseline parameters are extracted accordingly.

1009   Note that an epoch can only contain a single detected fish. The number of swim bouts ex-

1010   tracted from an epoch various extensively depending on the quality of the epoch (and behavior

1011   of fish). Having too many fish in the chamber may lead to low yields of aligned bouts despite

1012   having a large number of epochs. For details of fish detection, refer to Appendix 1.

1013 Export analyzed results

1014   Numerous attributes are saved as DataFrames under `keys` in HDF5 format files using our anal-

1015   ysis pipeline. Once the analysis is complete, three output data files are generated: `all_data.h5`,

1016   `bout_data.h5`, and `IEI_data.h5`.

1017   The `all_data.h5` file contains epoch-based data including raw data from DLM files, epoch

1018   attributes, baseline angular velocity, etc. The `bout_data.h5` file includes bout attributes and

1019   aligned bout data such as pitch angles and speed. The `IEI_data.h5` file contains all inter-event

1020   interval (IEI) data, or IBI. Refer to `docs/` for a complete list of saved attributes and their descrip-

1021   tion. In addition, a metadata table including recording frame rate, number of aligned bouts,

1022   and other information is generated and saved to the same directory.

1023   All results are saved as "long format" DataFrames with each row representing a time point or a

1024   bout/IEI, depending on the type of the result (one value per timepoint vs per bout/IBI). Values

1025   of multiple aligned bouts are stored in successive rows.

1026   All functions above can be called with script `src/SAMPL_analysis/SAMPL_analysis.py`. Refer

1027   to Appendix 5 for running instructions. For a record of analyzed files, frame rate, number of

1028   aligned bouts, etc., refer to the log file generated under `src/`.

1029 Load analyzed data and calculate parameters

1030   We include several plot functions under `src/SAMPL_visualization/` that calculate and plot all

1031   the parameters we report in the main text. These functions require an input of a root directory

1032   containing analyzed data. For recommended behavior data structure, see Appendix 5.

1033   Once data is found, plot functions get frame rate from metadata files and calculate the index

1034   of time of peak speed which is used to calculate the number of aligned frames and initialize

1035   other constants. Note that plot functions only read one frame rate for all the data to be plotted.

1036   Therefore, make sure all experiments are done at the same frame rate. To combine results from

1037   different frame rates for plotting, extract parameters of interest separately for experiments with

1038   different frame rates and concatenate the results afterwards. We only plot zeitgeber day data in

1039   this version of the code. Users may modify the `day_night_split()` function to extract zeitgeber

1040   night results if intended.

1041   To load analyzed swim bouts and IBI, we loop through all subfolders under the root directory

1042   and read DataFrames from HDF5 files, extract and calculate desired parameters and concate-

1043   nate results. Each plot function extracts parameters in different ways.

1044   For time series values to be plotted as a function of time, data is loaded from the `all_data.h5`

1045   file. The key `prop_bout_aligned` contains propulsive bouts that have been aligned and

1046   `grabbed_all` includes all epochs that contain swim bouts. See `plot_timeseries.py` for examples.

1047   Bout parameters, such as speed, displacement, pitch angles and attack angles, are also ex-

1048   tracted from `prop_bout_aligned` key containing aligned swim bouts. We use a dedicated func-

1049   tion for calculating these swim parameters: `extract_bout_features_v4()`. These parameters

1050   can be further used to get steering and righting gains. See `get_kinetics()` for more. Note that

1051   some parameters are determined by specific time points (such as initial pitch, post-bout pitch,

1052   etc.). To determine frames that are the closest to these time points, we use half round up for

1053   rounding.

1054   IBI data is loaded from the `IEI_data.h5` file under key `prop_bout_IEI2`. For bout tim-

1055   ing estimation, we calculate bout frequencies as reciprocals of bout intervals (IBIs). See

1056   `plot_bout_timing.py` and `plot_IBIposture.py` for examples.

1057   To calculate fin-body coordination, users need to determine how the `rotation` is calculated.

1058   One way is to use `rotation to time of peak angular velocity` which requires estimation of

1059   time of peak angular velocity. To do this, we first calculate angular velocity using smoothed

1060   pitch angles and adjust the signs so that values are positive before time of the peak speed.

1061   Median of angular velocity time series from the same experimental repeat (see Appendix 5

1062   for data organization) is used to find time of peak angular velocity. Lastly, we average results

1063   across experimental repeats to determine the peak angular velocity time. However, this calcu-

1064   lation requires a large amount of bout data. Alternatively, one may use a fixed value for time of

1065   peak angular velocity. Generally, we found -50 ms (50 ms before time of peak speed) to be a

1066   good value to use. Once the time of peak angular velocity is determined, rotation is calculated

1067   by pitch change from 250 ms before peak speed to time of peak angular velocity. Some scripts

1068   have the option to sample data from each experimental repeats. See Appendix 5 for instruc-

1069   tion.

Visualize results

We use the Seaborn package for data visualization [133]. Each plotting script generates a folder under `figures/` and saves figures as PDFs. Below is a list of available plotting functions and their descriptions. For more details, refer to the `README` document.

1. `plot_timeseries.py`

   plots basic parameters as a function of time. Modify `all_features` to select parameters to plot. This script contains two functions: `plot_aligned()`, `plot_raw()`. Change variable `all_features` to select parameters to plot.

2. `plot_parameters.py`

   plots swim parameter distribution and 2D distribution of parameters for kinetics calculation. This script contains function: `plot_parameters()`.

3. `plot_IBIposture.py`

   plots Inter Bout Interval (IBI; aka inter-event interval, IEI) posture distribution and standard deviation. This script contains function: `plot_IBIposture()`. This script looks for `prop_Bout_IEI2` in the `prop_bout_IEI_pitch` data which includes mean of body angles during IBI. When input root directory contains multiple experimental repeats, the scripts allows sampling of IBIs from each repeat by specifying argument `sample_bout`.

4. `plot_IBIposture.py`

   plots Inter Bout Interval (IBI; aka inter-event interval, IEI) posture distribution and standard deviation. This script contains function: `plot_IBIposture()`. This script looks for `prop_Bout_IEI2` in the `prop_bout_IEI_pitch` data which includes mean of body angles during IBI. When input root directory contains multiple experimental repeats, the scripts allows sampling of bouts from each repeat by specifying argument `sample_bout`.

5. `plot_bout_timing.py`

   Plots bout frequency as a function of IBI pitch and fitted coefficients of function. This script contains function: `plot_bout_frequency()`. When input root directory contains multiple experimental repeats, the scripts allows sampling of bouts from each repeat by specifying argument `sample_bout`.

6. `plot_kinematics.py`

1099   Plots righting gain, set point and steering gain. This script contains function:

1100   `plot_kinetics()`. When input root directory contains multiple experimental repeats, the

1101   scripts allows sampling of bouts from each repeat by specifying argument `sample_bout`.

1102   7. `plot_fin_body_coordination.py`

1103   Plots attack angle as a function of rotation and calculates fin-body ratio. Rotation is

1104   calculated by pitch change from -250 ms to -40 ms. This script contains function:

1105   `plot_fin_body_coordination()`. For reliable sigmoid regression, 6000+ bouts is recom-

1106   mended. When input root directory contains multiple experimental repeats, the scripts al-

1107   lows sampling of bouts from each repeat by specifying argument `sample_bout`.

1108   8. `plot_fin_body_coordination_byAngvelMax.py`

1109   Plots attack angle as a function of rotation and calculates fin-body ratio. Rotation is calcu-

1110   lated by pitch change from -250 ms to time of max angular velocity. For reliable sigmoid

1111   regression, 6000+ bouts is recommended. When input root directory contains multiple ex-

1112   perimental repeats, the scripts allows sampling of bouts from each repeat by specifying ar-

1113   gument `sample_bout`.

1114   **APPENDIX 5: STANDARD OPERATING PROCEDURE FOR RUNNING EXPERIMENTS AND**

1115   **ANALYZING DATA WITH SAMPL**

1116   In this appendix, we provide a step-by-step instruction for running experiments and analyzing

1117   SAMPL data. Refer to the Key Resources Table for access to SAMPL analysis and visualization

1118   scripts.

1119   **Experimental design**

1120   SAMPL experiments usually involve comparing behaviors of two or more groups of fish with

1121   different mutations, transgenic backgrounds, or manipulation. We suggest first deciding *a*

1122   *priori* on the total number of bouts required to resolve differences Figure 8 with the desired

1123   power. Typically, one SAMPL experimental repeat containing two 24-hour sessions using 3

1124   boxes with 5-7 larvae per box yields 3000-6000 bouts, which is usually sufficient for param-

1125   eter calculation Figure 8. However, multiple factors can affect data size per repeat, such as:

1126   manipulations (mutation/drug treatment), the throughput of manipulation, the availability of

1127   apparatuses, and the number of larvae with desired background per clutch. We therefore sug-

1128   gest running a pilot experiment first to determine the number of bouts that can be expected

1129   per box. Once done, we suggest defining an "experiment" with respect to the desired num-

1130   ber of bouts, which will specify the number of boxes and larvae per box required. Outlier boxes

1131   with too few or too many bouts (e.g. more/less than 2SD) can then be excluded from further

1132   analysis according to pre-determined criteria. Finally, we recommend running the full "exper-

1133   iment" multiple times to ensure that the findings are reproducible, and to report the variance

1134   across estimated parameters. Certain circumstances may be ill-suited to this approach: for ex-

1135   ample, if particular genotypes of larvae are especially rare, such as in the case of doubly biallelic

1136   mutants, or genotypes that simply swim drastically less. In such cases one can combine swim

1137   bouts across experimental repeats, and report the estimated error in parameter estimates us-

1138   ing statistical resampling techniques such as the jackknife.

1139   **Running an experiment**

1140   One typical SAMPL experimental repeat contains two 24-hour sessions. We suggest running

1141   zebrafish larvae at one of 3 time points: 4-6 dpf, 7-9 dpf, or 14-16 dpf. Larvae should be given

1142   30 minutes of access to food before being placed into chambers. We suggest putting 5-8 lar-

1143   vae into one standard chamber and 1-3 larvae in one narrow chamber to maximize data yield.

1144   Behavior recording requires having a single fish in the FOV at a time. Appearance of additional

1145   larvae will disrupt fish detection. We suggest transferring 25-30/10-15 ml E3 medium into

1146   each standard/narrow chamber to account for evaporation and maximize likelihood of fish

1147   swimming in the FOV. Throughput of the apparatus can be found in Figure 2 (standard cham-

1148   ber based on 58 larvae; narrow chamber based on 23 larvae).

1149   With SAMPL, one computer can control up to three behavioral apparatus, or "boxes." Once the

1150   fish chamber is put into the box and secured, open the program (Blue, Gold, Red) correspond-

1151   ing to the box to run on the computer controlling the boxes. Enter experimental information

1152   in the window opened: Genotype (experimental conditions), Cross ID, Fish number, etc. Set the

1153   destination folder for data storage. Choose the desired Light-Dark (L/D) cycle from one of the

1154   followings: L/D, L/L, or D/D. Adjust daytime light connection/timer accordingly. Use fish size

1155   toggle to select thresholds for fish detection: use `Small fish` for larvae younger than 12 dpf

1156   and `Big fish` for those that are older. To start recording, click `Select Background` when there's

1157   no fish in the FOV.

1158   Larvae older than 5 dpf should be fed every 24 hours with 1-2 ml of diluted cultured rotifers.

1159   To feed fish, click `Stop program` to stop the current session. Feed with rotifers and allow a pause

1160   of 30 min before re-starting the experiment.

1161   At the end of the experiment, click `Stop program` and remove fish from the box. Each session

1162 (from `Start` to `Stop program`) generates one `.dlm` data file and a corresponding `.ini` metadata

1163 file.

Software requirement for data analysis

1165 To analyze behavior data using code provided, one needs Python 3, analysis scripts, and vari-

1166 ous Python modules. An integrated development environment (IDE) is recommended to edit,

1167 debug, and run the code. If you don't have a personal preference, we recommend using Visual

1168 Studio Code (Microsoft). Analysis and visualization code was developed using Python 3. For the

1169 ease of package management, we suggest the use of environment management tools, such

1170 as miniconda.

1171 The most recent version of the code we use to analyze SAMPL data can be found online at

1172 https://. Download the entire directory by pressing the green Code button and downloading

1173 the ZIP file (orange box) so that you can make changes as needed for your project. The `src`

1174 folder contains all scripts. The `sample figures` folder contains examples of plots from the visu-

1175 alization functions. Please refer to the `README` for instructions and user guides.

1176 To set up a virtual environment, open a new terminal or use the terminal in your IDE, and type:

```
1177 conda create -n <myenv>
```

1178 where `<myenv>` is substituted with any desired name for the environment. Next, activate this

1179 environment

```
1180 conda activate <myenv>
```

1181 and install packages required for analysis and plotting using

```
1182 conda install <package>
```

1183 Below is a list of required packages[134-140] other than those included in Python 3.10.4:

```
1184 - astropy=5.1
1185 - pandas=1.4.4
1186 - pytables=3.7.0
1187 - matplotlib=3.5.2
1188 - numpy=1.23.3
1189 - scipy=1.9.1
```

1190   - `seaborn=0.12.0`

1191   - `tqdm=4.64.1`

1192   - `scikit-learn=1.1.1`

1193   For a complete list of packages, refer to the `environment.yml` file.

Bout analysis

1195   Analysis and plotting scripts support two types of data structures. The first option is one root

1196   directory containing all data files:

```
root
├── data1.dlm
├── data1 parameters.ini
├── data2.dlm
├── data2 parameters.ini
└── ...
```

1197   The second is a root directory containing subfolders with the necessary files indicating experi-

1198   mental repeats:

```
root
├── exp repeat 1
│   ├── data1.dlm
│   ├── data1 parameters.ini
│   ├── data2.dlm
│   ├── data2 parameters.ini
│   └── ...
├── exp repeat 2
│   ├── data1.dlm
│   ├── data1 parameters.ini
│   ├── data2.dlm
│   ├── data2 parameters.ini
│   └── ...
```

1199   Run the analysis script `.../src/SAMPL_analysis/SAMPL_analysis.py` and input data directory (di-

1200   rectory of the root folder) and the frame rate as instructed. This function aligns bouts in `.dlm`

1201   files within a directory so that peak speed is at time 0 ms, with 500 ms of activity before and

1202   300ms of activity after. It is important to note that all files in the same subfolders under the in-

1203   put directory will be combined to extract bout parameters. The analysis script will take the sub-

1204   mitted directory and analyze all data files within it, including all subfolders in its search, regard-

1205   less of depth. Subfolders can be used to separate analyses, experimental conditions, or repeats.

1206   Data with different frame rates should be analyzed separately to ensure proper parameter cal-

1207   culation, as only one can be used at a time.

1208   The program will skip the current `.dlm` file if it fails to detect a bout in it. However, errors are ex-

1209   pected if files contain too little recorded data to extract a bout. Therefore, we suggest removing

1210 any `.dlm` files that are smaller than 1 MB.

1211 When analysis is done, it will save three data files (`.h5`), four catalog files (`.csv`), and two meta-

1212 data files (`.csv`) under the same directory as the data is in. Below is an example of an analyzed

1213 directory:

```
root
├── data1.dlm
├── data1 parameters.ini
├── data2.dlm
├── data2 parameters.ini
├── all_data.h5
├── bout_data.h5
├── IEI_data.h5
├── analysis info.csv
├── root metadata.csv
├── catalog all_data.csv
├── catalog bout_data.csv
├── catalog IEI_data.csv
└── data_file_explained.csv
```

1214 Visualizing results

1215 After analysis, the scripts under the `visualization` folder are used to extract swim parameters

1216 and kinetics, and visualize them. For more detailes, refer to Appendix 4 and the README doc-

1217 ument. Each function can be run individually and will ask for the directory path to your data

1218 (see the Bout analysis section above). Alternatively, use `plot_all.py` to plot all figures.

1219 If the data size from a single repeat is not adequate for parameter calculation, we suggest com-

1220 bining data from multiple repeats and use sampling techniques such as Jackknifing for error

1221 estimation.

REFERENCES

1. Jorik Nonnekes, Rianne J. M. Goselink, Evžen Růžička, Alfonso Fasano, John G. Nutt, and Bastiaan R. Bloem. Neurological disorders of gait, balance and posture: a sign-based approach. *Nature Reviews Neurology*, 14(3):183–189, January 2018.

2. Saba Parvez, Chelsea Herdman, Manu Beerens, Korak Chakraborti, Zachary P. Harmer, Jing-Ruey J. Yeh, Calum A. MacRae, H. Joseph Yost, and Randall T. Peterson. MIC-drop: A platform for large-scale in vivo CRISPR screens. *Science*, 373(6559):1146–1151, September 2021.

3. Edward A Burton and Harold A Burgess. A critical review of zebrafish neurological disease models – 2. application: functional and neuroanatomical phenotyping strategies and chemical screens. *Oxford Open Neuroscience*, December 2022.

4. Kyle Honegger and Benjamin de Bivort. Stochasticity, individuality and behavior. *Current Biology*, 28(1):R8–R12, January 2018.

5. Roland S. Wu, Ian I. Lam, Hilary Clay, Daniel N. Duong, Rahul C. Deo, and Shaun R. Coughlin. A rapid method for directed gene knockout for screening in g0 zebrafish. *Developmental Cell*, 46(1):112–125.e4, July 2018.

6. William Joo, Michael D. Vivian, Brett J. Graham, Edward R. Soucy, and Summer B. Thyme. A customizable low-cost system for massively parallel zebrafish behavioral phenotyping. *Frontiers in Behavioral Neuroscience*, 14, January 2021.

7. Jessy Lauer, Mu Zhou, Shaokai Ye, William Menegas, Steffen Schneider, Tanmay Nath, Mohammed Mostafizur Rahman, Valentina Di Santo, Daniel Soberanes, Guoping Feng, Venkatesh N. Murthy, George Lauder, Catherine Dulac, Mackenzie Weygandt Mathis, and Alexander Mathis. Multi-animal pose estimation, identification and tracking with DeepLabCut. *Nature Methods*, 19(4):496–504, April 2022.

8. Pierre Karashchuk, Katie L. Rupp, Evyn S. Dickinson, Sarah Walling-Bell, Elischa Sanders, Eiman Azim, Bingni W. Brunton, and John C. Tuthill. Anipose: A toolkit for robust markerless 3d pose estimation. *Cell Reports*, 36(13):109730, September 2021.

9. Adam Gosztolai, Semih Günel, Victor Lobato-Ríos, Marco Pietro Abrate, Daniel Morales, Helge Rhodin, Pascal Fua, and Pavan Ramdya. LiftPose3d, a deep learning-based approach for transforming two-dimensional to three-dimensional poses in laboratory animals. *Nature Methods*, 18(8):975–981, August 2021.

10. Gordon J. Berman, William Bialek, and Joshua W. Shaevitz. Predictability and hierarchy in *Drosophila* behavior. *Proceedings of the National Academy of Sciences*, 113(42):11943–11948, October 2016.

11. Sandeep Robert Datta, David J. Anderson, Kristin Branson, Pietro Perona, and Andrew Leifer. Computational neuroethology: A call to action. *Neuron*, 104(1):11–24, October 2019.

12. Kevin Luxem, Jennifer J. Sun, Sean P. Bradley, Keerthi Krishnan, Eric A. Yttri, Jan Zimmermann, Talmo D. Pereira, and Mark Laubach. Open-source tools for behavioral video analysis: Setup, methods, and development. *arXiv*, 2022.

13. Michael B. Orger and Gonzalo G. de Polavieja. Zebrafish behavior: Opportunities and challenges. *Annual Review of Neuroscience*, 40(1):125–147, July 2017.

14. Eva M. Berg, E. Rebecka Björnfors, Irene Pallucchi, Laurence D. Picton, and Abdeljabbar El Manira. Principles governing locomotion in vertebrates: Lessons from zebrafish. *Frontiers in Neural Circuits*, 12, September 2018.

15. Martha W Bagnall and David Schoppik. Development of vestibular behaviors in zebrafish. *Current Opinion in Neurobiology*, 53:83–89, December 2018.

16. David E. Ehrlich and David Schoppik. Control of movement initiation underlies the development of balance. *Current Biology*, 27(3):334–344, February 2017.

17. David E. Ehrlich and David Schoppik. A novel mechanism for volitional locomotion in larval zebrafish. *bioRxiv*, September 2017.

18. David E Ehrlich and David Schoppik. A primal role for the vestibular sense in the development of coordinated locomotion. *eLife*, 8, October 2019.

19. Yuri Agrawal, John P. Carey, Charles C. Della Santina, Michael C. Schubert, and Lloyd B. Minor. Disorders of balance and vestibular function in US adults. *Archives of Internal Medicine*, 169(10):938, May 2009.

20. João C. Marques, Simone Lackner, Rita Félix, and Michael B. Orger. Structure of the zebrafish locomotor repertoire revealed with unsupervised behavioral clustering. *Current Biology*, 28(2):181–195.e5, January 2018.

21. S.A. Budick and D.M. O'Malley. Locomotor repertoire of the larval zebrafish: swimming, turning and prey capture. *Journal of Experimental Biology*, 203(17):2565–2579, September 2000.

22. Kristen E. Severi, Ruben Portugues, João C. Marques, Donald M. O'Malley, Michael B. Orger, and Florian Engert. Neural control and modulation of swimming speed in the larval zebrafish. *Neuron*, 83(3):692–707, August 2014.

23. Andrew D Bolton, Martin Haesemeyer, Josua Jordi, Ulrich Schaechtle, Feras A Saad, Vikash K Mansinghka, Joshua B Tenenbaum, and Florian Engert. Elements of a stochastic 3d prediction engine in larval zebrafish prey capture. *eLife*, 8, November 2019.

24. Yuri Glebovich Aleyev. *Nekton*. Dr. W. Junk, 1977.

25. P. W. Webb. Control of posture, depth, and swimming trajectories of fishes. *Integrative and Comparative Biology*, 42(1):94–101, February 2002.

26. Merlin Lange, Frederic Neuzeret, Benoit Fabreges, Cynthia Froc, Sebastien Bedu, Laure Bally-Cuif, and William H. J. Norton. Inter-individual and inter-strain variations in zebrafish locomotor ontogeny. *PLoS ONE*, 8(8):e70172, August 2013.

27. Zara Kanold-Tso and Dietmar Plenz. Variability of wheel running behavior in mice is dependent on housing, sex, and genetic background. *bioRxiv*, October 2022.

28. Lauren S. Bailey, Jared R. Bagley, Rainy Dodd, Ashley Olson, Mikayla Bolduc, Vivek M. Philip, Laura G. Reinholdt, Stacey J. Sukoff Rizzo, Lisa Tarantino, Leona Gagnon, Elissa J. Chesler, and James David Jentsch. Heritable variation in locomotion, reward sensitivity and impulsive behaviors in a genetically diverse inbred mouse panel. *Genes, Brain and Behavior*, 20(8), October 2021.

29. Liangyu Tao and Vikas Bhandawat. Mechanisms of variability underlying odor-guided locomotion. *Frontiers in Behavioral Neuroscience*, 16, May 2022.

30. Benjamin de Bivort, Sean Buchanan, Kyobi Skutt-Kakaria, Erika Gajda, Julien Ayroles, Chelsea O'Leary, Pablo Reimers, Jamilla Akhund-Zade, Rebecca Senft, Ryan Maloney, Sandra Ho, Zach Werkhoven, and Matthew A.-Y. Smith. Precise quantification of behavioral individuality from 80 million decisions across 183, 000 flies. *Frontiers in Behavioral Neuroscience*, 16, May 2022.

31. Florence Kermen, Lea Darnet, Christoph Wiest, Fabrizio Palumbo, Jack Bechert, Ozge Uslu, and Emre Yaksi. Stimulus-specific behavioral responses of zebrafish to a large range of odors exhibit individual variability. *BMC Biology*, 18(1), June 2020.

32. Jennifer A. Fitzgerald, Krishna Tulasi Kirla, Carl P. Zinner, and Colette M. vom Berg. Emergence of consistent intra-individual locomotor patterns during zebrafish development. *Scientific Reports*, 9(1), September 2019.

33. Carlos Pantoja, Adam Hoagland, Elizabeth C. Carroll, Vasiliki Karalis, Alden Conner, and Ehud Y. Isacoff. Neuromodulatory regulation of behavioral individuality in zebrafish. *Neuron*, 91(3):587–601, August 2016.

34. Ceyhan Ceran Serdar, Murat Cihan, Doğan Yücel, and Muhittin A Serdar. Sample size, power and effect size revisited: simplified and practical approaches in pre-clinical, clinical and laboratory studies. *Biochemia medica*, 31(1):27–53, February 2021.

35. Arseny Finkelstein, Liora Las, and Nachum Ulanovsky. 3-d maps and compasses in the brain. *Annual Review of Neuroscience*, 39(1):171–196, July 2016.

36. Daniel B. Turner-Evans, Kristopher T. Jensen, Saba Ali, Tyler Paterson, Arlo Sheridan, Robert P. Ray, Tanya Wolff, J. Scott Lauritzen, Gerald M. Rubin, Davi D. Bock, and Vivek Jayaraman. The neuroanatomical ultrastructure and function of a biological ring attractor. *Neuron*, 108(1):145–163.e10, October 2020.

37. Nikolai Bernstein. *The coordination and regulation of movements*. Pergamon, Oxford, 1967.

38. M. H. Dickinson. How animals move: An integrative view. *Science*, 288(5463):100–106, apr 2000.

39. H. J. Chiel, L. H. Ting, O. Ekeberg, and M. J. Z. Hartmann. The brain in its body: Motor control and sensing in a biomechanical context. *Journal of Neuroscience*, 29(41):12807–12814, oct 2009.

40. Esther Thelen. Motor development: A new synthesis. *American Psychologist*, 50(2):79–95, 1995.

41. S.J. Schnörr, P.J. Steenbergen, M.K. Richardson, and D.L. Champagne. Measuring thigmotaxis in larval zebrafish. *Behavioural Brain Research*, 228(2):367–374, March 2012.

42. Hidehiko K Inagaki, Azusa Kamikouchi, and Kei Ito. Methods for quantifying simple gravity sensing in *Drosophila melanogaster*. *Nature Protocols*, 5(1):20–25, December 2009.

43. Seymour Benzer. Behavioral mutants of *Drosophila* isolated by countercurrent distribution. *Proceedings of the National Academy of Sciences*, 58(3):1112–1119, September 1967.

44. Yishan Sun, Lei Liu, Yehuda Ben-Shahar, Julie S. Jacobs, Daniel F. Eberl, and Michael J. Welsh. TRPA channels distinguish gravity sensing from hearing in johnston's organ. *Proceedings of the National Academy of Sciences*, 106(32):13606–13611, August 2009.

45. Azusa Kamikouchi, Hidehiko K. Inagaki, Thomas Effertz, Oliver Hendrich, André Fiala, Martin C. Göpfert, and Kei Ito. The neural basis of drosophila gravity-sensing and hearing. *Nature*, 458(7235):165–171, March 2009.

46. Jerry Hirsch. Studies in experimental behavior genetics: II. individual differences in geotaxis as a function of chromosome variations in synthesized drosophila populations. *Journal of Comparative and Physiological Psychology*, 52(3):304–308, 1959.

47. Andrew M Seeds, Primoz Ravbar, Phuong Chung, Stefanie Hampel, Frank M Midgley, Brett D Mensh, and Julie H Simpson. A suppression hierarchy among competing motor programs drives sequential grooming in drosophila. *eLife*, 3, August 2014.

48. Giorgio F Gilestro. Video tracking and analysis of sleep in drosophila melanogaster. *Nature Protocols*, 7(5):995–1007, April 2012.

49. Philip Coen, Jan Clemens, Andrew J. Weinstein, Diego A. Pacheco, Yi Deng, and Mala Murthy. Dynamic sensory cues shape song structure in drosophila. *Nature*, 507(7491):233–237, March 2014.

50. Eleftheria Vrontou, Steven P Nilsen, Ebru Demir, Edward A Kravitz, and Barry J Dickson. fruitless regulates aggression and dominance in *Drosophila*. *Nature Neuroscience*, 9(12):1469–1471, November 2006.

51. Efrén Álvarez-Salvado, Angela M Licata, Erin G Connor, Margaret K McHugh, Benjamin MN King, Nicholas Stavropoulos, Jonathan D Victor, John P Crimaldi, and Katherine I Nagel. Elementary sensory-motor transformations underlying olfactory navigation in walking fruit-flies. *eLife*, 7, August 2018.

52. Marie P. Suver, Andrew M.M. Matheson, Sinekdha Sarkar, Matthew Damiata, David Schoppik, and Katherine I. Nagel. Encoding of wind direction by central neurons in drosophila. *Neuron*, 102(4):828–842.e7, May 2019.

53. Greg J. Stephens, Bethany Johnson-Kerner, William Bialek, and William S. Ryu. Dimensionality and dynamics in the behavior of c. elegans. *PLoS Computational Biology*, 4(4):e1000028, April 2008.

54. Quan Wen, Michelle D. Po, Elizabeth Hulme, Sway Chen, Xinyu Liu, Sen Wai Kwok, Marc Gershow, Andrew M. Leifer, Victoria Butler, Christopher Fang-Yen, Taizo Kawano, William R. Schafer, George Whitesides, Matthieu Wyart, Dmitri B. Chklovskii, Mei Zhen, and Aravinthan D.T. Samuel. Proprioceptive coupling within motor neurons drives *C. elegans* forward locomotion. *Neuron*, 76(4):750–761, November 2012.

55. Christopher Fang-Yen, Matthieu Wyart, Julie Xie, Risa Kawai, Tom Kodger, Sway Chen, Quan Wen, and Aravinthan D. T. Samuel. Biomechanical analysis of gait adaptation in the nematode *Caenorhabditis elegans*. *Proceedings of the National Academy of Sciences*, 107(47):20323–20328, November 2010.

56. Andrés Vidal-Gadea, Stephen Topper, Layla Young, Ashley Crisp, Leah Kressin, Erin Elbel, Thomas Maples, Martin Brauner, Karen Erbguth, Abram Axelrod, Alexander Gottschalk, Dionicio Siegel, and Jonathan T. Pierce-Shimomura. *Caenorhabditis elegans* selects distinct crawling and swimming gaits via dopamine and serotonin. *Proceedings of the National Academy of Sciences*, 108(42):17504–17509, October 2011.

57. Jonathan T. Pierce-Shimomura, Beth L. Chen, James J. Mun, Raymond Ho, Raman Sarkis, and Steven L. McIntire. Genetic analysis of crawling and swimming locomotory patterns in *C. elegans*. *Proceedings of the National Academy of Sciences*, 105(52):20982–20987, December 2008.

58. Jonathan T. Pierce-Shimomura, Thomas M. Morse, and Shawn R. Lockery. The fundamental role of pirouettes in *Caenorhabditis elegans* chemotaxis. *The Journal of Neuroscience*, 19(21):9557–9569, November 1999.

59. Jesse M. Gray, Joseph J. Hill, and Cornelia I. Bargmann. A circuit for navigation in *Caenorhabditis elegans*. *Proceedings of the National Academy of Sciences*, 102(9):3184–3191, February 2005.

60. Ikue Mori and Yasumi Ohshima. Neural regulation of thermotaxis in *Caenorhabditis elegans*. *Nature*, 376(6538):344–348, July 1995.

61. William S. Ryu and Aravinthan D. T. Samuel. Thermotaxis in *Caenorhabditis elegans* analyzed by measuring responses to defined thermal stimuli. *The Journal of Neuroscience*, 22(13):5727–5733, July 2002.

62. Y. Iino and K. Yoshida. Parallel use of two behavioral mechanisms for chemotaxis in caenorhabditis elegans. *Journal of Neuroscience*, 29(17):5370–5380, April 2009.

63. Aurélie Guisnet, Malosree Maitra, Sreeparna Pradhan, and Michael Hendricks. A three-dimensional habitat for c. elegans environmental enrichment. *PLOS ONE*, 16(1):e0245139, January 2021.

64. Wei-Long Chen, Hungtang Ko, Han-Sheng Chuang, David M. Raizen, and Haim H. Bau. *Caenorhabditis elegans* exhibits positive gravitaxis. *BMC Biology*, 19(1), September 2021.

65. Caroline Ackley, Neda Ziaei Kajbaf, Lindsey Washiashi, Ruchira Krishnamurthy, Pradeep Joshi, and Joel H. Rothman. Mechanosensory systems and sensory integration mediate *C. elegans* negative gravitaxis. *bioRxiv*, March 2022.

66. Caroline Ackley, Lindsey Washiashi, Ruchira Krishnamurthy, and Joel H. Rothman. Large-scale gravitaxis assay of *Caenorhabditis* dauer larvae. *Journal of Visualized Experiments*, 1(183), May 2022.

67. Florian A Dehmelt, Rebecca Meier, Julian Hinz, Takeshi Yoshimatsu, Clara A Simacek, Ruoyu Huang, Kun Wang, Tom Baden, and Aristides B Arrenberg. Spherical arena reveals optokinetic response tuning to stimulus location, size, and frequency across entire visual field of larval zebrafish. *eLife*, 10, June 2021.

68. C. Satou, Y. Kimura, T. Kohashi, K. Horikawa, H. Takeda, Y. Oda, and S. i. Higashijima. Functional role of a specialized class of spinal commissural inhibitory neurons during fast escapes in zebrafish. *Journal of Neuroscience*, 29(21):6780–6793, May 2009.

69. Yangzhong Zhou, Richard T Cattley, Clinton L Cario, Qing Bai, and Edward A Burton. Quantification of larval zebrafish motor function in multiwell plates using open-source MATLAB applications. *Nature Protocols*, 9(7):1533–1548, June 2014.

70. Carlos Pantoja, Adam Hoagland, Elizabeth Carroll, David Schoppik, and Ehud Isacoff. Measuring behavioral individuality in the acoustic startle behavior in zebrafish. *BIO-PROTOCOL*, 7(7), 2017.

71. Fabrizio Grieco, Ruud A.J. Tegelenbosch, and Lucas P.J.J. Noldus. Software tools for behavioral phenotyping of zebrafish across the life span. In *Behavioral and Neural Genetics of Zebrafish*, pages 527–550. Elsevier, 2020.

72. Justin J. Ingebretson and Mark A. Masino. Quantification of locomotor activity in larval zebrafish: considerations for the design of high-throughput behavioral studies. *Frontiers in Neural Circuits*, 7, 2013.

73. Harold A. Burgess and Michael Granato. Modulation of locomotor activity in larval zebrafish during light adaptation. *Journal of Experimental Biology*, 210(14):2526–2539, July 2007.

74. Arminda Suli, Glen M. Watson, Edwin W. Rubel, and David W. Raible. Rheotaxis in larval zebrafish is mediated by lateral line mechanosensory hair cells. *PLoS ONE*, 7(2):e29727, February 2012.

75. Raphaël Olive, Sébastien Wolf, Alexis Dubreuil, Volker Bormuth, Georges Debrégeas, and Raphaël Candelier. Rheotaxis of larval zebrafish: Behavioral study of a multi-sensory process. *Frontiers in Systems Neuroscience*, 10, February 2016.

76. Sophia Karpenko, Sebastien Wolf, Julie Lafaye, Guillaume Le Goc, Thomas Panier, Volker Bormuth, Raphaël Candelier, and Georges Debrégeas. From behavior to circuit modeling of light-seeking navigation in zebrafish larvae. *eLife*, 9, January 2020.

77. Kyle C Newton, Dovi Kacev, Simon R O Nilsson, Allison L Saettele, Sam A Golden, and Lavinia Sheets. Lateral line ablation by ototoxic compounds results in distinct rheotaxis profiles in larval zebrafish. *bioRxiv*, November 2021.

78. Eric Thomson, Mark Harfouche, Kanghyun Kim, Pavan Konda, Catherine W Seitz, Colin Cooke, Shiqi Xu, Whitney S Jacobs, Robin Blazing, Yang Chen, Sunanda Sharma, Timothy W Dunn, Jaehee Park, Roarke W Horstmeyer, and Eva A Naumann. Gigapixel imaging with a novel multi-camera array microscope. *eLife*, 11, December 2022.

79. Vilim Štih, Luigi Petrucco, Andreas M. Kist, and Ruben Portugues. Stytra: An open-source, integrated system for stimulation, tracking and closed-loop behavioral experiments. *PLOS Computational Biology*, 15(4):e1006699, April 2019.

80. Olivier Mirat, Jenna R. Sternberg, Kristen E. Severi, and Claire Wyart. ZebraZoom: an automated program for high-throughput behavioral analysis and categorization. *Frontiers in Neural Circuits*, 7, 2013.

81. Eva Sheardown, Aleksandra M. Mech, Maria Elena Miletto Petrazzini, Adele Leggieri, Agnieszka Gidziela, Saeedeh Hosseinian, Ian M. Sealy, Jose V. Torres-Perez, Elisabeth M. Busch-Nentwich, Margherita Malanchini, and Caroline H. Brennan. Translational relevance of forward genetic screens in animal models for the study of psychiatric disease. *Neuroscience & Biobehavioral Reviews*, 135:104559, April 2022.

82. Eric Wieschaus and Christiane Nüsslein-Volhard. The heidelberg screen for pattern mutants of *Drosophila*: A personal account. *Annual Review of Cell and Developmental Biology*, 32(1):1–46, October 2016.

83. Isabel Beets, Sven Zels, Elke Vandewyer, Jonas Demeulemeester, Jelle Caers, Esra Baytemur, William R. Schafer, Petra E. Vértes, Olivier Mirabeau, and Liliane Schoofs. System-wide mapping of neuropeptide-GPCR interactions in *C. elegans*. *bioRxiv*, November 2022.

84. Liang Ma, Yudan Zhao, Yuchen Chen, Biao Cheng, Anlin Peng, and Kun Huang. Caenorhabditis elegans as a model system for target identification and drug screening against neurodegenerative diseases. *European Journal of Pharmacology*, 819:169–180, January 2018.

85. Jason Henry and Donald Wlodkowic. High-throughput animal tracking in chemobehavioral phenotyping: Current limitations and future perspectives. *Behavioural Processes*, 180:104226, November 2020.

86. I. G. Woods, D. Schoppik, V. J. Shi, S. Zimmerman, H. A. Coleman, J. Greenwood, E. R. Soucy, and A. F. Schier. Neuropeptidergic signaling partitions arousal behaviors in zebrafish. *Journal of Neuroscience*, 34(9):3142–3160, February 2014.

87. Jason Rihel, David A. Prober, Anthony Arvanites, Kelvin Lam, Steven Zimmerman, Sumin Jang, Stephen J. Haggarty, David Kokel, Lee L. Rubin, Randall T. Peterson, and Alexander F. Schier. Zebrafish behavioral profiling links drugs to biological targets and rest/wake regulation. *Science*, 327(5963):348–351, January 2010.

88. David Kokel, Jennifer Bryan, Christian Laggner, Rick White, Chung Yan J Cheung, Rita Mateus, David Healey, Sonia Kim, Andreas A Werdich, Stephen J Haggarty, Calum A MacRae, Brian Shoichet, and Randall T Peterson. Rapid behavior-based identification of neuroactive small molecules in the zebrafish. *Nature Chemical Biology*, 6(3):231–237, January 2010.

89. Andrew J Rennekamp and Randall T Peterson. 15 years of zebrafish chemical screening. *Current Opinion in Chemical Biology*, 24:58–70, February 2015.

90. Pui-Ying Lam and Randall T Peterson. Developing zebrafish disease models for in vivo small molecule screens. *Current Opinion in Chemical Biology*, 50:37–44, June 2019.

91. Tejia Zhang and Randall T. Peterson. Zebrafish as a platform for drug screening. In *The Zebrafish in Biomedical Research*, pages 659–675. Elsevier, 2020.

92. E. Elizabeth Patton, Leonard I. Zon, and David M. Langenau. Zebrafish disease models in drug discovery: from preclinical modelling to clinical trials. *Nature Reviews Drug Discovery*, 20(8):611–628, June 2021.

93. I Litvan, C A Mangone, A McKee, M Verny, A Parsa, K Jellinger, L D'Olhaberriague, K R Chaudhuri, and R K Pearce. Natural history of progressive supranuclear palsy (steele-richardson-olszewski syndrome) and clinical predictors of survival: a clinicopathological study. *Journal of Neurology, Neurosurgery & Psychiatry*, 60(6):615–620, June 1996.

94. G. Respondek and G.U. Höglinger. The phenotypic spectrum of progressive supranuclear palsy. *Parkinsonism & Related Disorders*, 22:S34–S36, January 2016.

95. Carolin Kurz, Georg Ebersbach, Gesine Respondek, Armin Giese, Thomas Arzberger, and Günter Ulrich Höglinger. An autopsy-confirmed case of progressive supranuclear palsy with predominant postural instability. *Acta Neuropathologica Communications*, 4(1), November 2016.

96. Brent Bluett, Irene Litvan, Shumin Cheng, Jorge Juncos, David E. Riley, David G. Standaert, Stephen G. Reich, Deborah A. Hall, Benzi Kluger, David Shprecher, Connie Marras, and Joseph Jankovic. Understanding falls in progressive supranuclear palsy. *Parkinsonism & Related Disorders*, 35:75–81, February 2017.

97. Fraser S. Brown, James B. Rowe, Luca Passamonti, and Timothy Rittman. Falls in progressive supranuclear palsy. *Movement Disorders Clinical Practice*, 7(1):16–24, December 2019.

98. D R Williams. Predictors of falls and fractures in bradykinetic rigid syndromes: a retrospective study. *Journal of Neurology, Neurosurgery & Psychiatry*, 77(4):468–473, April 2006.

99. Jorik Nonnekes, Marjolein B. Aerts, W.F. Abdo, and Bastiaan R. Bloem. Medio-lateral balance impairment differentiates between parkinson's disease and atypical parkinsonism. *Journal of Parkinson's Disease*, 4(4):567–569, 2014.

100. Shinichi Amano, Jared W. Skinner, Hyo Keun Lee, Elizabeth L. Stegemöller, Nawaz Hack, Umer Akbar, David Vaillancourt, Nikolaus R. McFarland, and Chris J. Hass. Discriminating features of gait performance in progressive supranuclear palsy. *Parkinsonism & Related Disorders*, 21(8):888–893, August 2015.

101. Stefan Kammermeier, Kathrin Maierbeck, Lucia Dietrich, Annika Plate, Stefan Lorenzl, Arun Singh, Kai Bötzel, and Christoph Maurer. Qualitative postural control differences in idiopathic parkinson's disease vs. progressive supranuclear palsy with dynamic-on-static platform tilt. *Clinical Neurophysiology*, 129(6):1137–1147, June 2018.

102. Matthew D. Smith, Yoav Ben-Shlomo, and Emily Henderson. How often are patients with progressive supranuclear palsy really falling? *Journal of Neurology*, 266(8):2073–2074, May 2019.

103. Nicolina Goldschagg, Tatiana Bremova-Ertl, Stanislav Bardins, Nora Dinca, Katharina Feil, Siegbert Krafczyk, Stefan Lorenzl, and Michael Strupp. No evidence of a contribution of the vestibular system to frequent falls in progressive supranuclear palsy. *Journal of Clinical Neurology*, 15(3):339, 2019.

104. Marian L. Dale, Fay B. Horak, W. Geoffrey Wright, Bernadette M. Schoneburg, John G. Nutt, and Martina Mancini. Impaired perception of surface tilt in progressive supranuclear palsy. *PLOS ONE*, 12(3):e0173351, March 2017.

105. M. M. Traub, J. C. Rothwell, and C. D. Marsden. Anticipatory postural reflexes in parkinson's disease and other akinetic-rigid syndromes and in cerebellar ataxia. *Brain*, 103(2):393–412, 1980.

106. Louisa Murdin and Adolfo M. Bronstein. Head deviation in progressive supranuclear palsy: enhanced vestibulo-collic reflex or loss of resetting head movements? *Journal of Neurology*, 256(7):1143–1145, March 2009.

107. A. R. Bisdorff, A. M. Bronstein, C. Wolsley, and A. J. Lees. Torticollis due to disinhibition of the vestibulo-collic reflex in a patient with steele-richardson-olszewski syndrome. *Movement Disorders*, 12(3):328–336, May 1997.

108. Stefan Kammermeier, Lucia Dietrich, Kathrin Maierbeck, Annika Plate, Stefan Lorenzl, Arun Singh, and Kai Bötzel. Neck vibration proprioceptive postural response intact in progressive supranuclear palsy unlike idiopathic parkinson's disease. *Frontiers in Neurology*, 8, December 2017.

109. A. Tanigawa, A. Komiyama, and O. Hasegawa. Truncal muscle tonus in progressive supranuclear palsy. *Journal of Neurology, Neurosurgery & Psychiatry*, 64(2):190–196, February 1998.

110. William Ondo, Deborah Warrior, Averell Overby, Janine Calmes, Nancy Hendersen, Sharon Olson, and Joseph Jankovic. Computerized posturography analysis of progressive supranuclear palsy. *Archives of Neurology*, 57(10), October 2000.

111. K. Liao, J. Wagner, A. Joshi, I. Estrovich, M. F. Walker, M. Strupp, and R. J. Leigh. Why do patients with PSP fall?: Evidence for abnormal otolith responses. *Neurology*, 70(10):802–809, jan 2008.

112. Ke Liao, Mark F. Walker, Anand Joshi, Millard Reschke, Michael Strupp, and R. John Leigh. The human vertical translational vestibulo-ocular reflex. *Annals of the New York Academy of Sciences*, 1164(1):68–75, May 2009.

113. Athena L. Chen, David E. Riley, Susan A. King, Anand C. Joshi, Alessandro Serra, Ke Liao, Mark L. Cohen, Jorge Otero-Millan, Susana Martinez-Conde, Michael Strupp, and R. John Leigh. The disturbance of gaze in progressive supranuclear palsy: Implications for pathogenesis. *Frontiers in Neurology*, 1, 2010.

114. Ke Liao, Mark F. Walker, Anand C. Joshi, Millard Reschke, Michael Strupp, Judith Wagner, and R. John Leigh. The linear vestibulo-ocular reflex, locomotion and falls in neurological disorders. *Restorative Neurology and Neuroscience*, 28(1):91–103, 2010.

115. Jeroen Venhovens, Jan Meulstee, Bas R. Bloem, and Wim I. M. Verhagen. Neurovestibular dysfunction and falls in parkinson's disease and atypical parkinsonism: A prospective 1 year follow-up study. *Frontiers in Neurology*, 11, October 2020.

116. Jonathan J. Sager, Gonzalo E. Torres, and Edward A. Burton. The zebrafish homologue of the human DYT1 dystonia gene is widely expressed in CNS neurons but non-essential for early motor system development. *PLoS ONE*, 7(9):e45175, September 2012.

117. L. Flinn, H. Mortiboys, K. Volkmann, R. W. Koster, P. W. Ingham, and O. Bandmann. Complex i deficiency and dopaminergic neuronal cell loss in parkin-deficient zebrafish (danio rerio). *Brain*, 132(6):1613–1623, May 2009.

118. Laura J. Flinn, Marcus Keatinge, Sandrine Bretaud, Heather Mortiboys, Hideaki Matsui, Elena De Felice, Helen I. Woodroof, Lucy Brown, Aimee McTighe, Rosemarie Soellner, Claire E. Allen, Paul R. Heath, Marta Milo, Miratul M. K. Muqit, Andreas S. Reichert, Reinhard W. Köster, Philip W. Ingham, and Oliver Bandmann. TigarBcauses mitochondrial dysfunction and neuronal loss in PINK1 deficiency. *Annals of Neurology*, 74(6):837–847, December 2013.

119. Ville Sallinen, Juha Kolehmainen, Madhusmita Priyadarshini, Gabija Toleikyte, Yu-Chia Chen, and Pertti Panula. Dopaminergic cell damage and vulnerability to MPTP in pink1 knockdown zebrafish. *Neurobiology of Disease*, 40(1):93–101, October 2010.

120. Qing Bai, Steven J. Mullett, Jessica A. Garver, David A. Hinkle, and Edward A. Burton. Zebrafish DJ-1 is evolutionarily conserved and expressed in dopaminergic neurons. *Brain Research*, 1113(1):33–44, October 2006.

121. T. L. Henshall, B. Tucker, A. L. Lumsden, S. Nornes, M. T. Lardelli, and R. I. Richards. Selective neuronal requirement for huntingtin in the developing zebrafish. *Human Molecular Genetics*, 18(24):4830–4842, September 2009.

122. H. Diekmann, O. Anichtchik, A. Fleming, M. Futter, P. Goldsmith, A. Roach, and D. C. Rubinsztein. Decreased BDNF levels are a major contributor to the embryonic phenotype of huntingtin knockdown zebrafish. *Journal of Neuroscience*, 29(5):1343–1349, February 2009.

123. William A. Campbell, Hongwei Yang, Henrik Zetterberg, Stéphanie Baulac, Jacqueline A. Sears, Tianming Liu, Stephen T. C. Wong, Tao P. Zhong, and Weiming Xia. Zebrafish lacking alzheimer presenilin enhancer 2 (pen-2) demonstrate excessive p53-dependent apoptosis and neuronal loss. *Journal of Neurochemistry*, 96(5):1423–1440, February 2006.

124. Tuan Leng Tay, Olaf Ronneberger, Soojin Ryu, Roland Nitschke, and Wolfgang Driever. Comprehensive catecholaminergic projectome analysis reveals single-neuron integration of zebrafish ascending and descending dopaminergic systems. *Nature Communications*, 2(1), January 2011.

125. Su Guo, Stephen W. Wilson, Sam Cooke, Ajay B. Chitnis, Wolfgang Driever, and Arnon Rosenthal. Mutations in the zebrafish unmask shared regulatory pathways controlling the development of catecholaminergic neurons. *Developmental Biology*, 208(2):473–487, April 1999.

126. Young-Ki Bae, Shuichi Kani, Takashi Shimizu, Koji Tanabe, Hideaki Nojima, Yukiko Kimura, Shin ichi Higashijima, and Masahiko Hibi. Anatomy of zebrafish cerebellum and screen for mutations affecting its development. *Developmental Biology*, 330(2):406–426, June 2009.

127. Francesca Peri and Christiane Nüsslein-Volhard. Live imaging of neuronal degradation by microglia reveals a role for v0-ATPase a1 in phagosomal fusion in vivo. *Cell*, 133(5):916–927, May 2008.

128. Simon RO Nilsson, Nastacia L. Goodwin, Jia Jie Choong, Sophia Hwang, Hayden R Wright, Zane C Norville, Xiaoyu Tong, Dayu Lin, Brandon S. Bentzley, Neir Eshel, Ryan J McLaughlin, and Sam A. Golden. Simple behavioral analysis (SimBA) – an open source toolkit for computer classification of complex social behaviors in experimental animals. *bioRxiv*, April 2020.

129. Sydney Brenner. The genetics of *Caenorhabditis elegans*. *Genetics*, 77(1):71–94, May 1974.

130. Harold A. Burgess and Michael Granato. Modulation of locomotor activity in larval zebrafish during light adaptation. *Journal of Experimental Biology*, 210(14):2526–2539, July 2007.

131. Harold A. Burgess and Michael Granato. Sensorimotor gating in larval zebrafish. *The Journal of Neuroscience*, 27(18):4984–4994, May 2007.

132. Said Pertuz, Domenec Puig, and Miguel Angel Garcia. Analysis of focus measure operators for shape-from-focus. *Pattern Recognition*, 46(5):1415–1432, May 2013.

133. Michael L. Waskom. seaborn: statistical data visualization. *Journal of Open Source Software*, 6(60):3021, 2021.

134. The Astropy Collaboration, Adrian M. Price-Whelan, Pey Lian Lim, Nicholas Earl, Nathaniel Starkman, Larry Bradley, David L. Shupe, Aarya A. Patil, Lia Corrales, C. E. Brasseur, Maximilian Nöthe, Axel Donath, Erik Tollerud, Brett M. Morris, Adam Ginsburg, Eero Vaher, Benjamin A. Weaver, James Tocknell, William Jamieson, Marten H. van Kerkwijk, Thomas P. Robitaille, Bruce Merry, Matteo Bachetti, H. Moritz Günther, Paper Authors, Thomas L. Aldcroft, Jaime A. Alvarado-Montes, Anne M. Archibald, Attila Bódi, Shreyas Bapat, Geert Barentsen, Juanjo Bazán, Manish Biswas, Médéric Boquien, D. J. Burke, Daria Cara, Mihai Cara, Kyle E Conroy, Simon Conseil, Matthew W. Craig, Robert M. Cross, Kelle L. Cruz, Francesco DEugenio, Nadia Dencheva, Hadrien A. R. Devillepoix, Jörg P. Dietrich, Arthur Davis Eigenbrot, Thomas Erben, Leonardo Ferreira, Daniel Foreman-Mackey, Ryan Fox, Nabil Freij, Suyog Garg, Robel Geda, Lauren Glattly, Yash Gondhalekar, Karl D. Gordon, David Grant, Perry Greenfield, Austen M. Groener, Steve Guest, Sebastian Gurovich, Rasmus Handberg, Akeem Hart, Zac Hatfield-Dodds, Derek Homeier, Griffin Hosseinzadeh, Tim Jenness, Craig K. Jones, Prajwel Joseph, J. Bryce Kalmbach, Emir Karamehmetoglu, Mikoaj Kauszyski, Michael S. P. Kelley, Nicholas Kern, Wolfgang E. Kerzendorf, Eric W. Koch, Shankar Kulumani, Antony Lee, Chun Ly, Zhiyuan Ma, Conor MacBride, Jakob M. Maljaars, Demitri Muna, N. A. Murphy, Henrik Norman, Richard OSteen, Kyle A. Oman, Camilla Pacifici, Sergio Pascual, J. Pascual-Granado, Rohit R. Patil, Gabriel I Perren, Timothy E. Pickering, Tanuj Rastogi, Benjamin R. Roulston, Daniel F Ryan, Eli S. Rykoff, Jose Sabater, Parikshit Sakurikar, Jesús Salgado, Aniket Sanghi, Nicholas Saunders, Volodymyr Savchenko, Ludwig Schwardt, Michael Seifert-Eckert, Albert Y. Shih, Anany Shrey Jain, Gyanendra Shukla, Jonathan Sick, Chris Simpson, Sudheesh Singanamalla, Leo P. Singer, Jaladh Singhal, Manodeep Sinha, Brigitta M. Sipcz, Lee R. Spitler, David Stansby, Ole Streicher, Jani umak, John D. Swinbank, Dan S. Taranu, Nikita Tewary, Grant R. Tremblay, Miguel de Val-Borro, Samuel J. Van Kooten, Zlatan Vasovi, Shresth Verma, José Vinícius de Miranda Cardoso, Peter K. G. Williams, Tom J. Wilson, Benjamin Winkel, W. M. Wood-Vasey, Rui Xue, Peter Yoachim, Chen Zhang, Andrea Zonca, and Astropy Project Contributors. The astropy project: Sustaining and growing a community-oriented open-source project and the latest major release (v5.0) of the core package*. *The Astrophysical Journal*, 935(2):167, aug 2022.

135. Wes McKinney et al. Data structures for statistical computing in python. In *Proceedings of the 9th Python in Science Conference*, volume 445, pages 51–56. Austin, TX, 2010.

136. PyTables Developers Team. PyTables: Hierarchical datasets in Python, 2002–.

137. Charles R. Harris, K. Jarrod Millman, Stéfan J. van der Walt, Ralf Gommers, Pauli Virtanen, David Cournapeau, Eric Wieser, Julian Taylor, Sebastian Berg, Nathaniel J. Smith, Robert Kern, Matti Picus, Stephan Hoyer, Marten H. van Kerkwijk, Matthew Brett, Allan Haldane, Jaime Fernández del Río, Mark Wiebe, Pearu Peterson, Pierre Gérard-Marchant, Kevin Sheppard, Tyler Reddy, Warren Weckesser, Hameer Abbasi, Christoph Gohlke, and Travis E. Oliphant. Array programming with NumPy. *Nature*, 585(7825):357–362, September 2020.

138. Pauli Virtanen, Ralf Gommers, Travis E. Oliphant, Matt Haberland, Tyler Reddy, David Cournapeau, Evgeni Burovski, Pearu Peterson, Warren Weckesser, Jonathan Bright, Stéfan J. van der Walt, Matthew Brett, Joshua Wilson, K. Jarrod Millman, Nikolay Mayorov, Andrew R. J. Nelson, Eric Jones, Robert Kern, Eric Larson, C J Carey, İlhan Polat, Yu Feng, Eric W. Moore, Jake VanderPlas, Denis Laxalde, Josef Perktold, Robert Cimrman, Ian Henriksen, E. A. Quintero, Charles R. Harris, Anne M. Archibald, Antônio H. Ribeiro, Fabian Pedregosa, Paul van Mulbregt, Aditya Vijaykumar, Alessandro Pietro Bardelli, Alex Rothberg, Andreas Hilboll, Andreas Kloeckner, Anthony Scopatz, Antony Lee, Ariel Rokem, C. Nathan Woods, Chad Fulton, Charles Masson, Christian Häggström, Clark Fitzgerald, David A. Nicholson, David R. Hagen, Dmitrii V. Pasechnik, Emanuele Olivetti, Eric Martin, Eric Wieser, Fabrice Silva, Felix Lenders, Florian Wilhelm, G. Young, Gavin A. Price, Gert-Ludwig Ingold, Gregory E. Allen, Gregory R. Lee, Hervé Audren, Irvin Probst, Jörg P. Dietrich, Jacob Silterra, James T Webber, Janko Slavič, Joel Nothman, Johannes Buchner, Johannes Kulick, Johannes L. Schönberger, José Vinícius de Miranda Cardoso, Joscha Reimer, Joseph Harrington, Juan Luis Cano Rodríguez, Juan Nunez-Iglesias, Justin Kuczynski, Kevin Tritz, Martin Thoma, Matthew Newville, Matthias Kümmerer, Maximilian Bolingbroke, Michael Tartre, Mikhail Pak, Nathaniel J. Smith, Nikolai Nowaczyk, Nikolay Shebanov, Oleksandr Pavlyk, Per A. Brodtkorb, Perry Lee, Robert T. McGibbon, Roman Feldbauer, Sam Lewis, Sam Tygier, Scott Sievert, Sebastiano Vigna, Stefan Peterson, Surhud More, Tadeusz Pudlik, Takuya Oshima, Thomas J. Pingel, Thomas P. Robitaille, Thomas Spura, Thouis R. Jones, Tim Cera, Tim Leslie, Tiziano Zito, Tom Krauss, Utkarsh Upadhyay, Yaroslav O. Halchenko, and Yoshiki Vázquez-Baeza and. SciPy 1.0: fundamental algorithms for scientific computing in python. *Nature Methods*, 17(3):261–272, February 2020.

139. Casper O. da Costa-Luis. tqdm: A fast, extensible progress meter for python and CLI. *Journal of Open Source Software*, 4(37):1277, May 2019.

140. F. Pedregosa, G. Varoquaux, A. Gramfort, V. Michel, B. Thirion, O. Grisel, M. Blondel, P. Prettenhofer, R. Weiss, V. Dubourg, J. Vanderplas, A. Passos, D. Cournapeau, M. Brucher, M. Perrot, and E. Duchesnay. Scikit-learn: Machine learning in Python. *Journal of Machine Learning Research*, 12:2825–2830, 2011.

Table 1: List of parts, prices per 12/2022

Computer & software licenses ($2,300; one computer runs three apparatus)

RAM (64GB)	Amazon B0884TNHNC
Case (small form factor)	Amazon B08BF8YMXC
Motherboard (Mini-ITX, AM4 CPU slot, on-board NIC)	Amazon B089D34SZT
Solid state hard drive (1TB)	Amazon B08V83JZH4
CPU w/embedded GPU (AMD Ryzen 7)	Amazon B091J3NYVF
Quiet CPU fan (Noctua)	Amazon B075SG1T3X
Power supply (450W)	Amazon B07DTP6SLJ
USB card	Amazon B08B5BNZQ6
Operating system (Windows 10 Professional)	Amazon B00ZSHDJ4O
Vision Development License (Image Processing)	National Instuments 778044-35
Vision Acquisition License (Image Acquisition)	National Instruments 778413-35
Software Runtime Engine	NI LabView Runtime (free download)

Shelving unit for 12 apparatus, ($2,100)

KVM switch to share keyboard, mouse and monitor w/cables	Amazon B001V9LQ52
Monitor 1920x1080	Amazon B07F8XZN69
Keyboard	Amazon B00CYX26BC
Mouse	Amazon B087Z733CM
Mobile wire shelving unit w/4 shelves 36"x81.5"x24"	McMaster Carr 2563T336
Extra shelf (handy to hold UPS and network gear up top)	McMaster Carr 5101T497
Uninterruptible power supply	Amazon B078D6KZ98
Spare battery for UPS (handy to have around)	Amazon B010XF8SCI
Timer (for light/dark)	Need 4, Amazon B005MMSTNG
Power strip (6', higher shelves, 2pk)	Amazon B082DVCCDR
Power strip (12', lower shelves, 2pk)	Amazon B08KZGT258
Wire ties (cable management)	Amazon B096ZHHRC3
Network cables CAT6a 10G 7ft (5pk & 10pk)	Amazon B01BGV2T5U
Network switch (Netgear GS110MX)	Amazon B076642YPN

Networked data storage ($3,800)

500GB solid state drive for data server caching	Need 2 Amazon B07M7Q21N7
Data server Synology DS1621xs+	Amazon B08HYRYLPS
16TB Hard drives for data server. Order 7 (6+1spare)	Need 7 Amazon B07SPFPKF4
10GB NIC for data server	Amazon B07G9N9KJT

Enclosure (BaseLabTools/Amazon/MetalsCut4U, $375 per apparatus)

Breadboard (see image w/measurements)	SABCUST
Rails for enclosure (see measurements)	X2020-CUST
Hardboard for enclosure walls (see measurements)	X2020-HB-CUST
Right angle joiner for LED strip	Need 2 X2020-AB1
Joiner cube for enclosure	X2020-C3W
Spring-loaded t-nuts (10pk)	X2020-DTSB-M5-P10
M5-0.8 x 8mm Screws	Amazon B07H18YDYB
Top: G90 galvanized steel (7.25in x 20.25in x 3in, 20 Ga.)	Tray, MetalsCut4U

ThorLabs parts ($550 per apparatus)

Holds condenser	SM2L05
Condenser/diffuser for IR light	ACL5040U-DG6-B
Tube to distance condenser from LED	SM2L20
Adapts IR light holder to post	SM2RC
Adapts SM2 tube to SM1 tube	SM1A2
Tube to hold heatsink	SM1M10
Adapts heatsink / LED to SM1 tube	SM1A6FW
Adapts camera to SM1 tube	SM1A10
Adapts SM1 tube to imaging lens	SM1A9
Filter to pass only IR light	FGL830
Adapts camera/lens to post	SM1RC
Holds filter / allows camera/lens mounting	SM1L03

Holds imaging chamber	Need 2 FP01
Post-holder for chamber holder / IR assembly	Need 3 PH1
Posts for chamber holder / IR assembly	Need 3 TR1
Post-holder for camera/lens	PH1.5
Post for camera/lens	TR1.5
1/4-20" screws to attach post-holder to breadboard	SH25S038
1/4-20" low-profile screws for enclosure	SH25LP38

IR LED (assembly required, $100 per apparatus)

12V 2A power supply for IR	Amazon B00Q2E5IXW
XT60H connector for IR lights	Amazon B09ST768W2
940nm 2.6V IR LED Opulent LST1-01F09-IR04-00	Mouser 416-LST101F09IR0400
Thermal epoxy (attach heatsink to ThorLabs SM1A6FW	Amazon B08Z73HH23
Ohmite heat sink	Mouser SV-LED-325E
HexaTherm tape (attach LED to heatsink)	LEDSupply A001
BuckBlock 1A	LEDSupply 0A009-D-V-1000

Daylight LED, ($50 for three apparatus)

12V 1A power supply for daytime lights (5pk)	Amazon B00FEOB4EI
SMD5050 6500K white LED 12V light strip 60LED/meter	Amazon B075R4X1XL
DC power pigtail (to connect LED strip to power)	Amazon B0768V9V5Q
T tap connectors	Amazon B085XGYW1B

Imaging, ($1,200-$1,800 per apparatus)

Camera (IMX174 chip, USB 3 interface)	e.g. Basler acA1920-155um
Lens (50mm, VIS-NIR coating)	Edmund Optics 67-717
USB cable	e.g. Edmund Optics 86-770

Chambers, laser cut by Pololu ($200)

Chamber sides	12mm (10.2 - 12.75mm) #2025 black cast acrylic, opaque
Chamber faces	1.5mm (0.8 - 2.1mm) clear cast acrylic
Weld-On 4 acrylic cement & applicator	Amazon B00TCUJ7A8

Table 2: Recording parameters for different organisms

	Zebrafish $\leq$ 12 dpf	Zebrafish > 12 dpf	*Drosophila*	*C. elegans*
Body low	14	14	100	20
Body high	255	255	255	255
Head low	45	45	30	21
Head high	255	255	255	255
Initial cut low	25	25	45	3
Initial cut high	120	120	145	30
Size low	180	250	80	30
Size high	260	450	180	80

Table 3: Measured parameters of posture and locomotion across development

| Parameter	Unit	4 dpf	7 dpf	14 dpf	Format	Definition
Peak speed	mm/s	10.42 (3.85)	13.02 (4.99)	11.41 (4.20)	Mean of bouts (SD)	Peak speed of swim bouts
Initial pitch	deg	5.21 (31.49)	0.77 (21.81)	0.54 (18.64)	Median of bouts (IQR)	Pitch angle at 250 ms before the peak speed
Pitch at peak speed	deg	9.74 (29.16)	6.84 (20.35)	4.36 (19.73)	Median of bouts (IQR)	Pitch angle at time of the peak speed
Post-bout pitch	deg	10.57 (23.86)	10.21 (16.70)	6.88 (16.05)	Median of bouts (IQR)	Pitch angle at 100 ms after the peak speed
End pitch	deg	10.85 (23.59)	10.78 (16.79)	7.56 (15.55)	Median of bouts (IQR)	Pitch angle at 200 ms after the peak speed
Bout trajectory	deg	12.29 (27.52)	8.92 (20.19)	7.85 (22.89)	Mean of bouts (SD)	Peak trajectory, tangential angle of the trajectory at the time of the peak speed
Bout displacement	mm	1.12 (0.63)	1.36 (0.64)	1.35 (0.70)	Mean of bouts (SD)	Average displacement of fish during a bout when speed is greater than 5 mm/s
Inter-bout interval	s	1.78 (2.61)	1.89 (2.75)	2.13 (2.80)	Median of bouts (IQR)	IBI, duration between two adjacent swim bouts
Bout frequency	Hz	0.56 (0.70)	0.53 (0.69)	0.47 (0.59)	Median of bouts (IQR)	Frequency of swim bouts determined by the reciprocal of inter-bout interval
IBI pitch	deg	8.75 (17.73)	8.06 (13.07)	6.08 (11.24)	Mean of bouts (SD)	Mean pitch angle during inter-bout interval
IBI pitch standard deviation	deg	17.48 (1.60)	12.66 (1.80)	11.23 (1.28)	Mean of repeats (SD)	Standard deviation of IBI pitch, a measurement of stability
Sensitivity	mHz/deg^2	0.61 (0.18)	1.06 (0.23)	1.31 (0.34)	Mean of repeats (SD)	Sensitivity to pitch changes. Determined by the coefficient of the quadratic term of the parabola model for bout timing
Baseline bout rate	Hz	0.51 (0.06)	0.51 (0.08)	0.47 (0.11)	Mean of repeats (SD)	Y intersect of the parabola model for bout timing
Trajectory deviation	deg	5.46 (14.53)	4.13 (11.57)	4.35 (16.39)	Mean of bouts (SD)	Deviation of bout trajectory from initial pitch
Steering rotation	deg	2.30 (7.51)	3.00 (7.33)	1.94 (6.31)	Mean of bouts (SD)	Change of pitch angle from initial (250 ms before) to the time of the peak speed
Steering gain	-	0.64 (0.04)	0.67 (0.04)	0.51 (0.05)	Mean of repeats (SD)	Slope of best fitted line of posture vs trajectory at the time of the peak speed
Steering-related rotation	deg	1.72 (6.15)	1.74 (5.95)	0.99 (5.42)	Mean of bouts (SD)	Change of pitch angle from initial to the time of max angular velocity
Attack angle	deg	4.10 (16.16)	0.77 (9.68)	0.91 (5.25)	Median of bouts (IQR)	Deviation of bout trajectory from pitch at time of the peak speed
Peak angular velocity time	ms	50.60 (7.62)	39.16 (4.96)	50.00 (5.12)	Mean of repeats (SD)	Time of peak angular velocity in ms before time of the peak speed
Fin-body ratio	-	3.41 (0.86)	2.27 (0.76)	3.55 (1.98)	Mean of repeats (SD)	Maximal slope of best fitted sigmoid of attack angle vs early rotation
Sigmoid height	deg	16.47 (2.31)	10.28 (1.78)	25.15 (4.68)	Mean of repeats (SD)	Height of best fitted sigmoid of attack angle vs early rotation
Righting rotation	deg	0.92 (3.49)	2.64 (3.55)	1.90 (3.01)	Mean of bouts (SD)	Change of pitch angle from time of the peak speed to post bout (100 ms after peak speed)
Righting gain	-	0.15 (0.02)	0.18 (0.02)	0.18 (0.02)	Mean of repeats (SD)	Numeric inversion of the slope of best fitted line of righting rotation vs initial pitch
Set point	deg	13.00 (2.10)	19.47 (2.28)	13.60 (1.78)	Mean of repeats (SD)	X intersect of best fitted line of righting rotation vs initial pitch
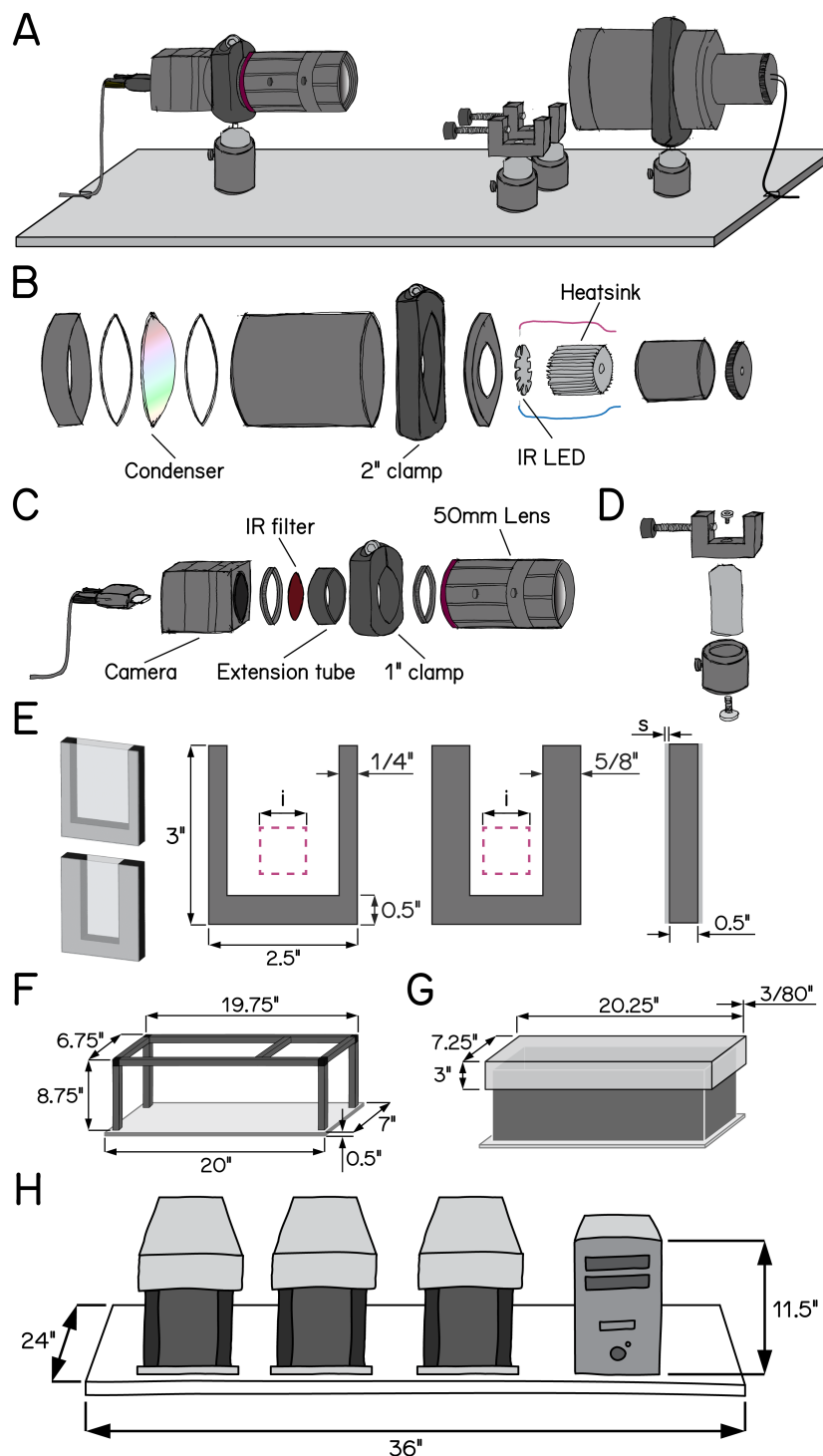
Figure 1: Schematic illustrations of SAMPL hardware design.
(A) Overview of the apparatus without aluminum rails, side panels, and the top panel. Equipment modules mounted on the breadboard are, from left to right, IR camera and lens, chamber holders, and IR illumination module.
(B) Exploded-view drawing of the IR illumination module.
(C) Exploded-view drawing of the camera and lens module.
(D) Exploded-view drawing of a chamber holder
(E) Design of fish chambers. From left to right: 3D illustration of a standard chamber (upper) and a narrow chamber (lower); front view of the u-shaped acrylic middle piece for the chambers; side view of the chamber. Pink squares illustrate the recording field of view. i = 20 mm; s = 1.5 mm.
(F) Dimensions of the apparatus frame and breadboard.
(G) Design and dimensions of the apparatus lid.
(H) Schematic illustration of a set of three SAMPL apparatus and a small-form-factor computer case on a 24"x36" shelf.
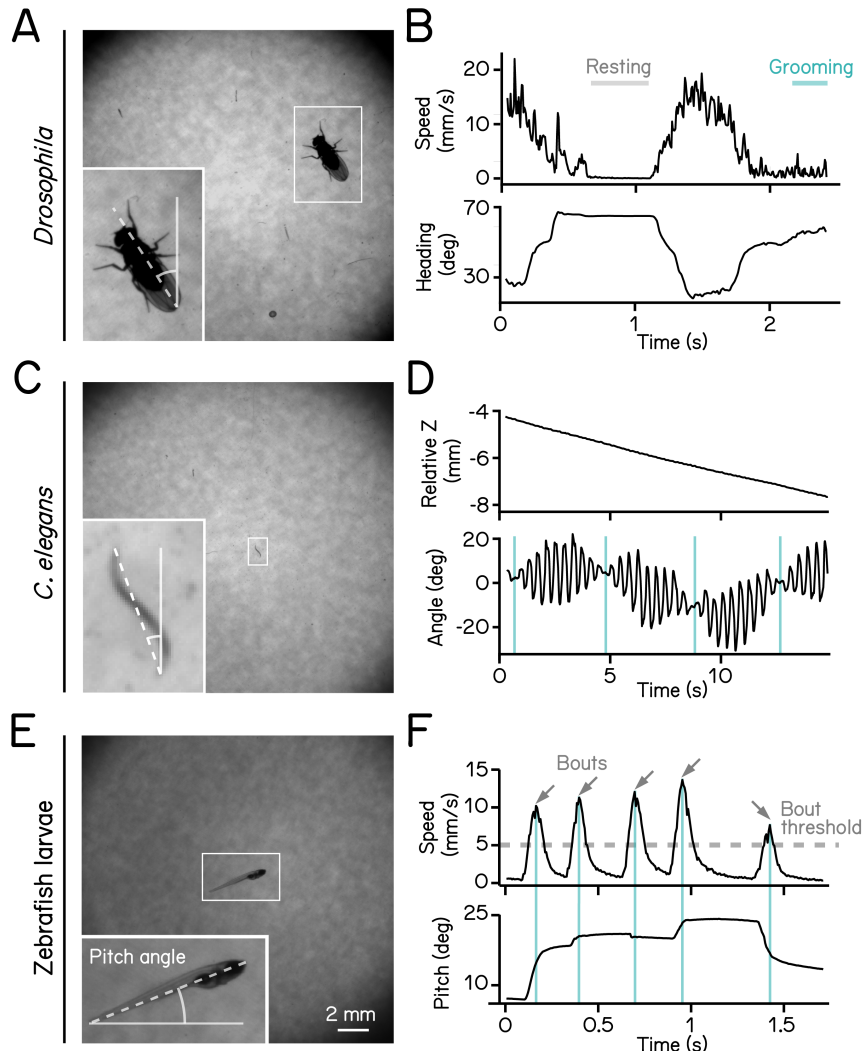
Figure 2: High-definition recording and measurement of animal locomotion using SAMPL.
(A) Example of a recorded frame with a *Drosophila melanogaster* (white box) in the SAMPL apparatus. Dashed line indicates heading of the fly relative to vertical up (north). Imaging was performed at 166 Hz with 1200×1216 pixels. Same as follows.
(B) Example of an epoch of a walking fly. Walking speed and heading are plotted as a function of time. Gray and cyan lines marks resting and grooming period, respectively (Movie 2).
(C) Example of a recorded frame with a *Caenorhabditis elegans* (white box) in the SAMPL apparatus. Dashed line indicates approximated angle of the worm relative to vertical.
(D) Example of an epoch of a swimming worm. Z position and approximated angle are plotted as a function of time. Cyan vertical lines label the time when the plane of movement is perpendicular to the imaging plane (Movie 2).
(E) Example of a recorded frame with a 7 dpf *Danio rerio* larva (white box) in the SAMPL apparatus. Pitch angle is determined as the angle of the trunk of the fish (dashed line) relative to horizontal. Positive pitch indicates nose-up posture whereas negative pitch represents nose-down posture.
(F) Example of an epoch containing multiple swim bouts (arrows). Swim speed and pitch angles are plotted as a function of time. Dashed line marks the 5 mm/s threshold for bout detection. Cyan vertical lines label time of the peak speed for each bout (Movie 3).
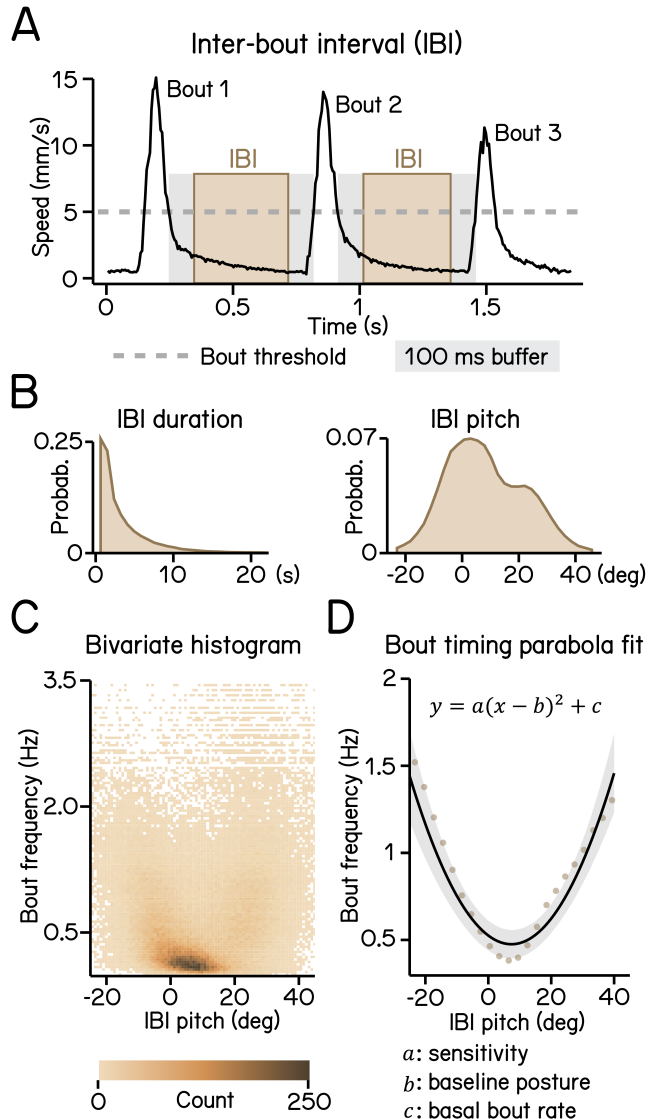
Figure 3: Modeling timing of swim bouts reveals larval sensitivity to pitch changes.
(A) An inter-bout interval (IBI, brown area) is defined as the duration when swim speed is below the 5 mm/s homeostasis threshold (dashed line) between two consecutive bouts with a 100 ms buffer window (grey area) deducted from each end.
(B) Distribution of IBI duration (left) and mean pitch angle during IBI (right).
(C) Bivariate histogram of bout frequency and IBI pitch. Bout frequency is the reciprocal of IBI duration.
(D) Bout frequency plotted as a function of IBI pitch and modeled with a parabola (black line, $R^2 = 0.14$). Brown dots indicate binned average of IBI pitch and bout frequencies calculated by sorting IBI pitch into 3°-wide bins. For all panels, n = 109593 IBIs from 537 fish over 27 repeats.
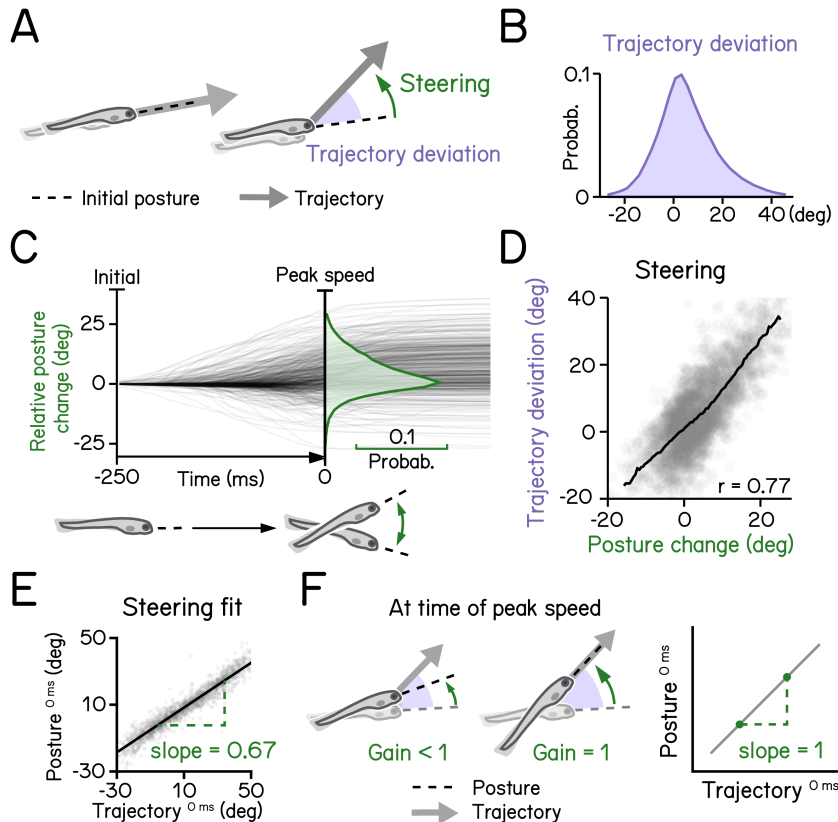
Figure 4: Larval vertical navigation is led by steering toward trajectory

(A) Schematic illustration of two climbing mechanics: (1) a larva may generate a thrust (arrow) toward the pointing direction (dashed line) at the initial of a bout (left); (2) a larva can steer (green arrow) toward an eccentric angle before the thrust (right). The offset between trust angle and the direction the larva point toward at bout initial is termed trajectory deviation (purple).

(B) Distribution of trajectory deviation.

(C) Changes of pitch angles relative to initial pitch plotted as a function of time (dark lines) overlaid with distribution of pitch change at time of peak speed (green).

(D) Trajectory deviation (purple) plotted as a function of posture changes from bout initial to time of the peak speed (green). Black line indicates binned average values. Positive correlation between trajectory deviation and posture change demonstrates that larvae steer toward the trajectory of the bout.

(E) To measure the gain of steering compared to trajectory deviation, pitch angels at time of the peak speed are plotted as a function of trajectory. Steering gain is determined as the slope of the fitted line (Pearson's r = 0.96).

(F) Schematic illustrations demonstrating how steering gain associates steering (green arrows) with trajectory deviation (purple). For all panels, n = 121979 bouts from 537 fish over 27 repeats.
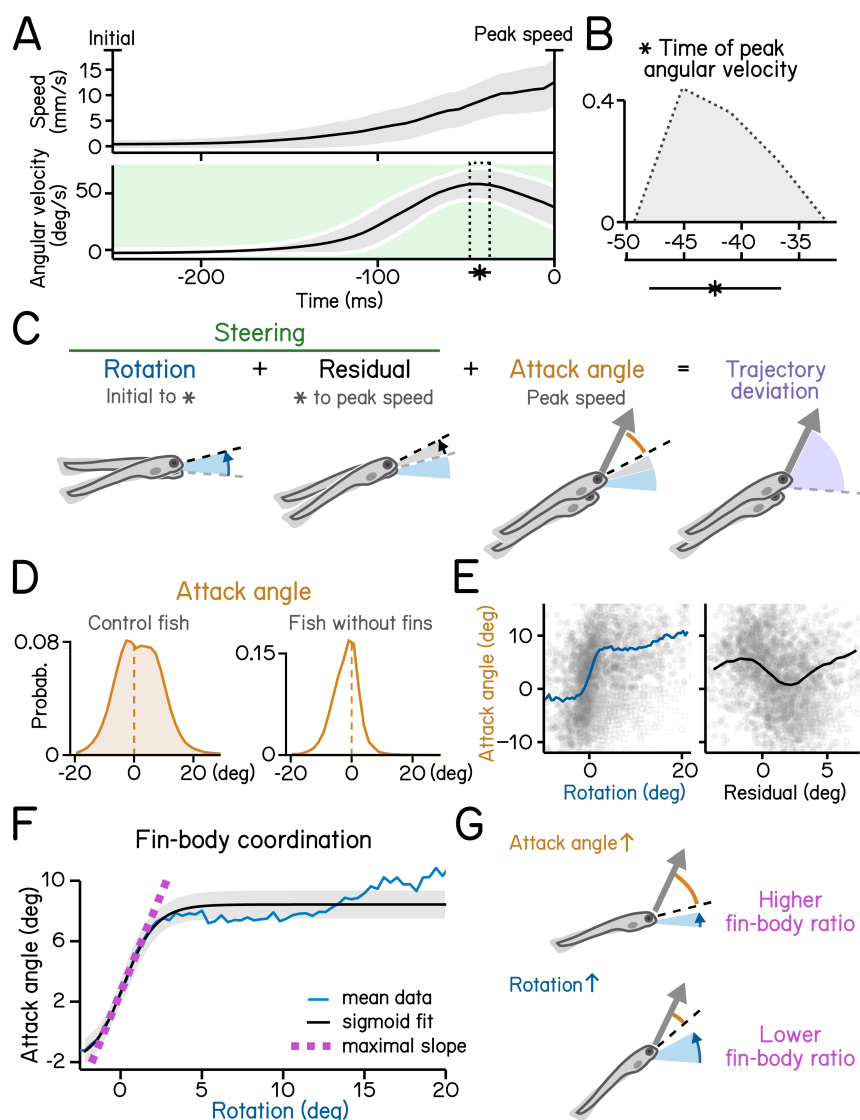
Figure 5: Steering requires coordination of fin and body.
(A) Swim speed (top) and angular velocity (bottom) plotted as a function of time. Angular velocity peaks (asterisk and dotted area, mean±SD) during steering phase (green) before time of the peak speed. Angular velocity is adjusted by flipping signs of bouts with nose-down rotations during steering (mean±SD across experimental repeats). Shaded region in the upper panel indicates mean±SD across all quantified swim bouts.
(B) Histogram of time of peak angular velocity, binned by frame, across experimental repeats with mean±SD plotted below.
(C) Illustration of components that contribute to trajectory deviation. Larvae rotate their bodies starting from bout initial (blue) and reach peak angular velocity (asterisk) before peak speed. Any rotation generated during decrease of angular velocity is considered residual (grey). At time of peak speed, there is an offset between the pitch angle (dashed line) and bout trajectory (arrow) which is termed attack angle (orange). Body rotations, residual, and attack angle add up to trajectory deviation.
(D) Distribution of attack angles in control fish (left) and fish after fin amputation (right). Dashed lines indicate 0 attack angle.
(E) Attack angles plotted as a function of body rotations (left, blue) or residual rotations (right). Rotations and residuals are sorted into 0.5°-wide bins for calculation of binned average attack angles. Swim bouts with negative attack angles while having steering rotations greater the 50th percentile (hollow squares) were excluded for binned-average calculation.
(F) Attack angles plotted as a function of body rotations (blue line) and fitted with a logistic model (black line, R^2 = 0.31). Fin-body ratio is determined by the slope of the maximal slope of the fitted sigmoid (magenta). Rotations are sorted into 0.8°-wide bins for calculation of binned average rotations and attack angles (blue line). Swim bouts with negative attack angles while having steering rotations greater the 50th percentile were excluded for sigmoid modeling.
(G) Schematic illustration of how fin-body ratio reflect climbing mechanics. For all panels, n = 121979 bouts from 537 fish over 27 repeats.
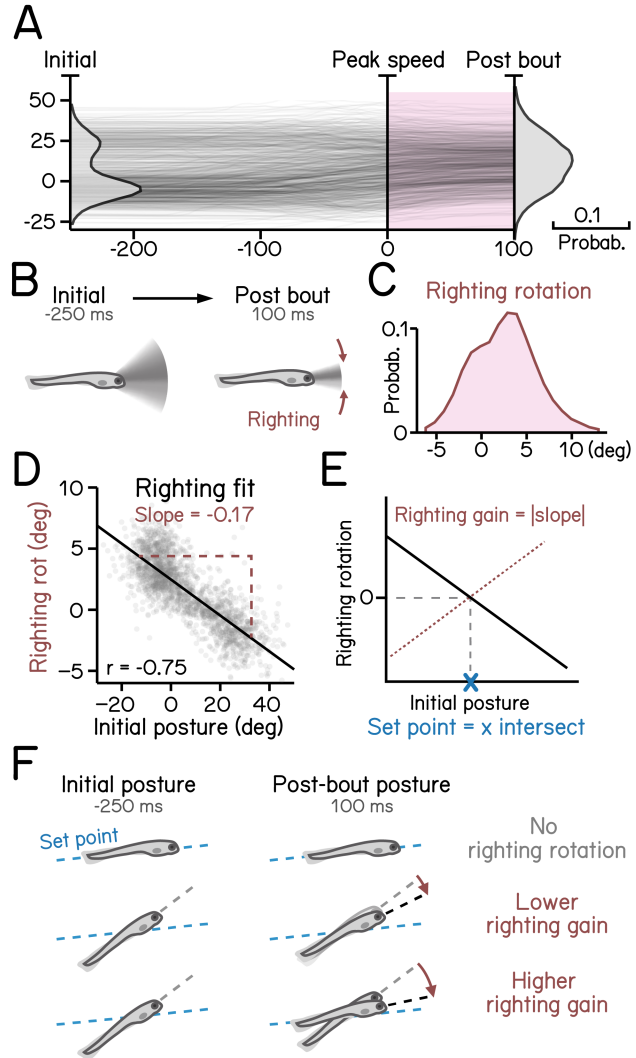
Figure 6: Righting rotation restores posture after peak speed.

(A) Pitch angles plotted as a function of time (dark lines) overlaid with distribution of pitch angles before (left) and after bouts (right). Red area indicates duration after peak speed when pitch distribution narrowed.

(B) Illustration of righting behavior. Larvae rotate (red arrows) toward more neutral posture after peak speed.

(C) Distribution of rotation during righting (red in **A**).

(D) Righting rotation plotted as a function of initial pitch angles.

(E) Righting gain is determined by the absolute value of the slope (red dotted line) of best fitted line (black line). The x intersect of the fitted line determines the set point (blue cross) indicating posture at which results in no righting rotation.

(F) Schematic illustration of righting rotation (red arrows), righting gain, and set point (blue dashed line). For all panels, n = 121979 bouts from 537 fish over 27 repeats.
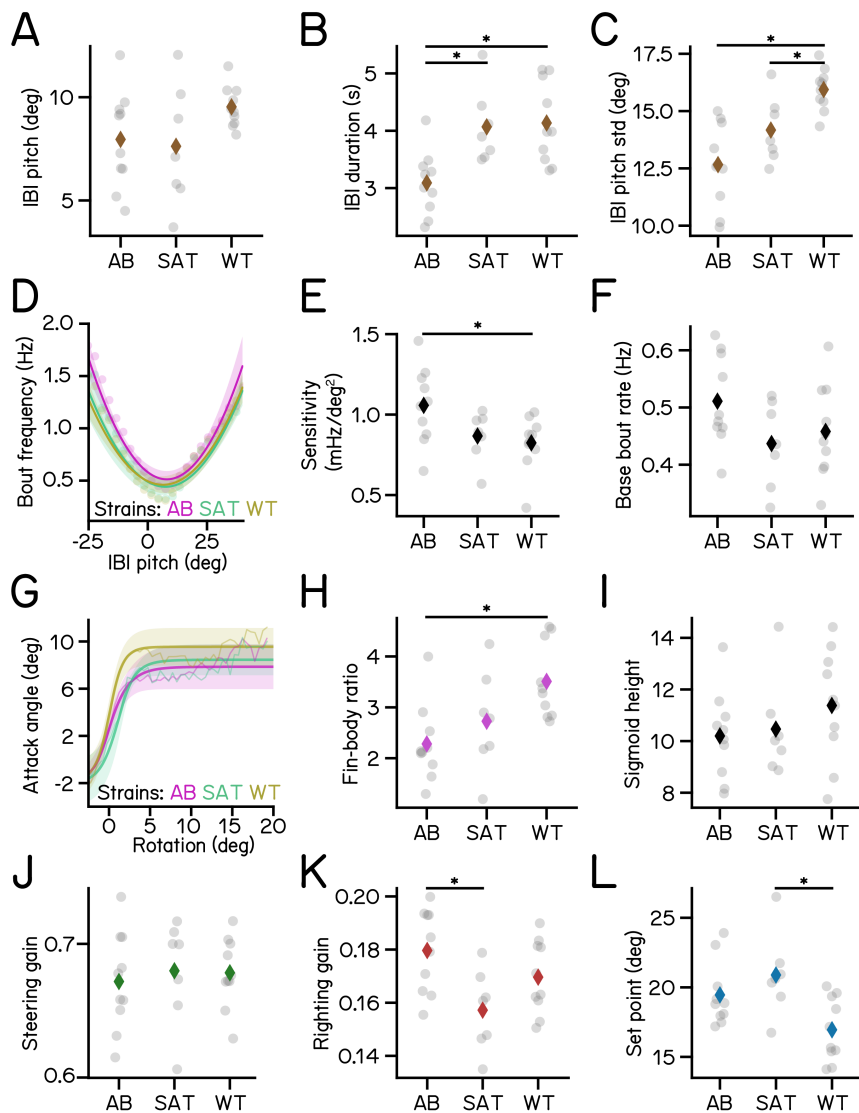
Figure 7: Variations of kinematic parameters among three different zebrafish strains.

(A) Average pitch angles during IBI.

(B) IBI duration (AB vs SAT p-adj = 0.0128; AB vs WT p-adj = 0.0034).

(C) Standard deviation of IBI pitch (AB vs WT p-adj = 0.0001; SAT vs WT p-adj = 0.0479).

(D) Bout frequency plotted as a function of IBI pitch modeled with parabolas.

(E) Sensitivity to pitch changes (AB vs WT p-adj = 0.0319).

(F) Baseline bout rate.

(G) Attack angles plotted as a function of body rotations modeled with sigmoids.

(H) Fin-body ratio (AB vs WT p-adj = 0.0066).

(I) Height of the sigmoid in **G**.

(J) Steering gain of different strains.

(K) Righting gain of different strains (AT vs SAT p-adj = 0.0133).

(L) Set point (SAT vs WT p-adj = 0.0094). For each strain of AB/SAT/WT, N = 10/7/10 repeats, n = 62457/27990/31532 bouts and 55683/25964/27946 IBIs from 225/117/195 fish.
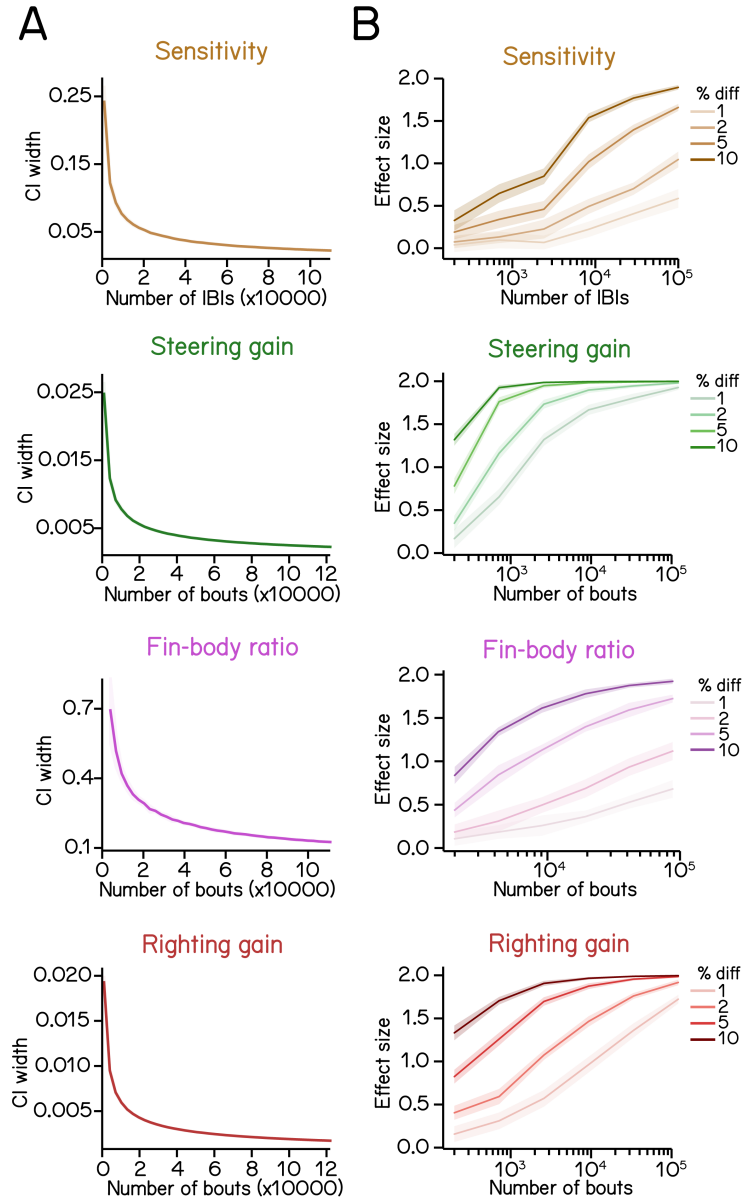
Figure 8: Statistics of regression analysis for swim kinematics.
(A) Confidence interval (CI) width of kinematic parameters plotted as a function of sample size at 0.95 significance level (mean ± SD as ribbon). Errors were estimated by resampling with replacement from the complete dataset. (B) Effect size plotted as a function of sample size at various percentage differences. Refer to Methods for details of computation.
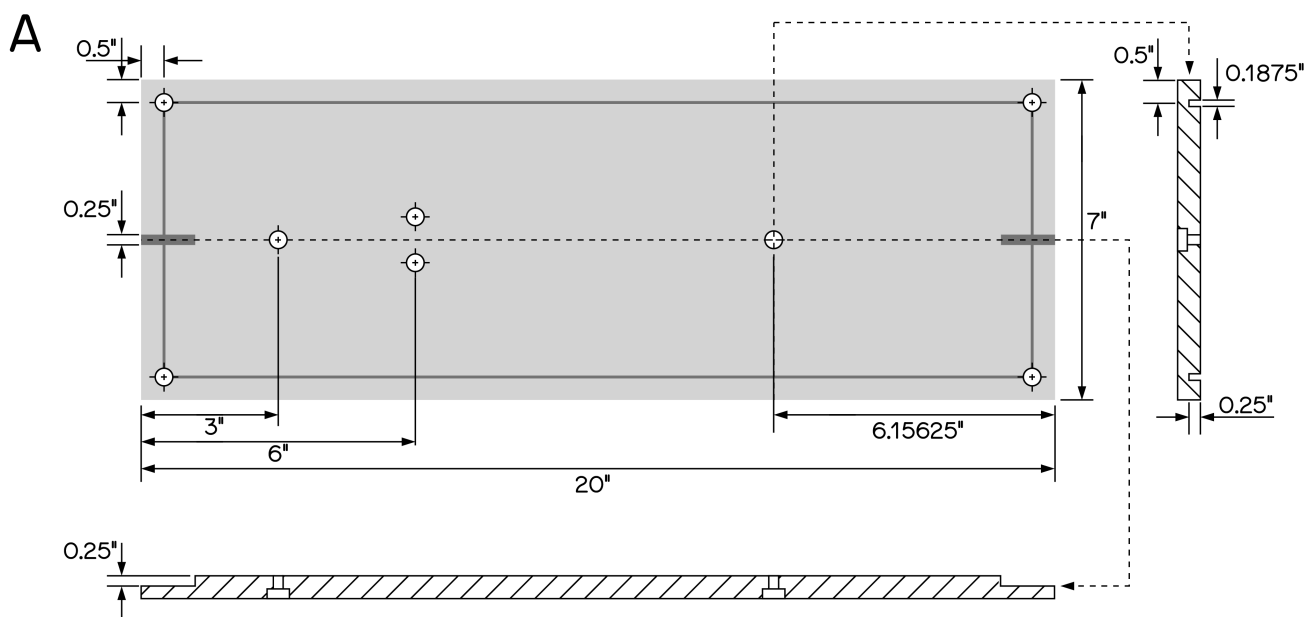
Figure S1: Custom breadboard for SAMPL base
(A) Custom aluminum breadboard, not anodized, 0.5" thick. All holes (8 total) counterbored for 1/4"-20 cap screw. Grooves to be cut on the side of the breadboard OPPOSITE to the counterbore.